Microstructures and quartz lattice-preferred orientations in the eclogite-bearing migmatitic gneisses of the D'Entrecasteaux Islands, Papua New Guinea

T. A. Little
School of Geography, Environment & Earth Sciences, Victoria University of Wellington, New Zealand (tim.little@vuw.ac.nz)

B. R. Hacker, S. J. Brownlee, and G. Seward
Earth Research Institute, University of California − Santa Barbara, Santa Barbara, California, USA

[1] Lattice preferred orientations (LPO) of quartz in gneiss domes of the D'Entrecasteaux Islands, Woodlark Rift shed insight into exhumation of the world's youngest (~5–7 Ma) eclogite-bearing terrane at cm/yr rates. We focus on deformation that affected the terrane as it transited between lower crustal depths and the surface, including: (1) grain-scale deformation mechanisms; and (2) style of flow and mode of emplacement of the domes. Electron-backscatter diffraction was used to analyze microstructure and LPOs of 37 quartzofeldspathic gneiss samples that enclose meter-scale mafic blocks preserving original eclogite-facies assemblages. During exhumation of the ultrahigh-pressure (UHP) terrane, gneisses were retrogressed in the amphibolite facies at lower crustal depths. The LPOs change from dome cores to carapaces, consistent with decreasing deformational temperatures. In the relatively chilled outer carapaces of the domes, the quartz LPOs consist of mostly crossed-girdle [c]-axis patterns, with some cleft-girdle and small-circle LPOs, and record dislocation creep accommodated by mixed-$<a>$ slip. In the cores of the migmatitic domes, a chessboard pattern of subgrains is common, and quartz LPOs primarily record prism-[c] slip, probably at $>630\,°C$. Other microstructures indicate recovery by high-temperature grain-boundary migration. Grain-boundary mobility was anisotropic, leading to strong grain-shape fabrics oblique to foliation, but not obviously relatable to shear sense. Evidence for melt-present deformation is abundant, and microstructures (including partially dissolved feldspar grains) indicate some deformation by fluid-assisted grain-boundary diffusion creep. LPOs in carapace rocks are symmetrical, recording flow that was dominantly coaxial. We interpret the gneiss domes to have been emplaced into the rift as partially molten diapirs.

1. Introduction

[2] During the past two decades many high-pressure (HP) and ultrahigh-pressure (UHP) metamorphic terranes of various ages have been identified in the orogenic belts of the world [e.g., *Ernst*, 2001], raising questions about the rheology of deeply subducted continental materials and the tectonic processes that carried them back to Earth's surface [e.g., *Hacker*, 1996; *Stöckhert*, 2002; *Lenze and Stöckhert*, 2007]. The Pliocene eclogite-bearing gneiss domes in the Woodlark Rift of SE Papua New Guinea (PNG) [*Ollier and Pain*, 1980; *Davies and Warren*, 1988] expose the world's youngest known eclogite-bearing terrane [*Baldwin et al.*, 2004; *Ota and Koneko*, 2010] (Figure 1). Their tectonic burial began in the Paleogene as a result of the northward subduction of the thinned northern Australian continental margin (mostly Cretaceous) in the Papuan subduction zone near the SW edge of the current SE PNG mainland (Papuan Orogen, Figure 1b). During this convergence the Papuan Ultramafic body (PUB) (an ophiolite up to 12 km thick, *Davies and Jaques*, 1984) was emplaced SW-ward over a subduction complex derived from sediments and volcanic rocks that had been scraped of the Australian Plate [*Lus et al.*, 2004; *Davies*, 2012]. Today the terrane is exposed in the upper plate of the former Papuan subduction zone in a central part of the Woodlark Rift. The eclogite-bearing terrane is remarkable because it is exposed in an active continental rift that hosted its rapid unroofing from mantle to crustal depths. Following metamorphic crystallization of the terrane at 7–4 Ma, the deeply subducted, mostly felsic composition rocks rose—essentially isothermally—at cm/yr rates from depths of >90 km (in the case of the coesite-bearing mafic eclogite boudins) [*Hill and Baldwin*, 1993; *Baldwin et al.*, 2004; *Monteleone et al.*, 2007; *Baldwin et al.*, 2008]. Thermobarometry and U-Pb dating of zircon indicates that the rocks reached lower crustal depths of ~35 km (~11 kb) by circa 3.5 Ma [*Hill and Baldwin*, 1993; *Gordon et al.*, 2012]. There, the UHP terrane stalled for ~1 Myr was retrogressed in the upper amphibolite facies, and ductilely deformed, acquiring a foliation that extended subhorizontally across the extent of the current D'Entrecasteaux Islands [*Little et al.*, 2011; *Gordon et al.*, 2012]. Except in the unaltered cores of mafic boudins, the mineralogical and fabric record of the earlier eclogite-facies history of the rocks was largely removed as a result of the retrogression.

Between 3.5 and 2.4 Ma, vertical thinning of the terrane was accompanied by partial melting of the gneisses to form migmatites and by intrusion of abundant syntectonic granitoids [*Gordon et al.*, 2012]. How early (or at what depth) melting of the gneisses may have begun remains uncertain. By ~2 – 1.5 Ma, a final pulse of exhumation had carried the migmatitic gneisses to the upper crust to form gneiss domes [*Baldwin & Ireland*, 1995; *Hill & Baldwin* 1993; *Gordon et al.*, 2012]. $^{40}Ar/^{39}Ar$ and fission-track thermochronology indicates cooling of the rocks below ~400 °C at rates of >100 ° C/Myr [*Baldwin et al.*, 1993].

[3] The above exhumation scenario has been supported by recent geodynamical models. *Ellis et al.* [2011] showed that partial melting of the gneisses during decompression could have enhanced the density contrast of the felsic gneisses to the mantle, and also dramatically reduced their viscosity—with both effects helping to drive a rapid buoyant ascent of the UHP terrane. At the same time, isostatic buoyancy forces related to extensional thinning in the overlying Woodlark rift further promoted exhumation of the terrane: with some parts breaching the surface, and others at depth flowing laterally parallel to the rift margins [*Ellis et al.*, 2011].

[4] The final phase of exhumation precipitated rapid cooling of the partially molten gneiss domes, quenching their high-temperature microstructures, and sheltering them from later static recrystallization. In this paper, we have studied the remarkably youthful and well-preserved deformational fabrics in the rocks to gain insight into: (1) deformation mechanisms affecting rapidly exhuming, partially molten continental crust; and (2) the kinematics of gneiss dome emplacement into the crust—a process that here contributed to exhumation of a UHP eclogite-bearing terrane. We ask, was syn-exhumational deformation of the eclogite-bearing terrane at crustal depths detachment driven, involving a dominance of non-coaxial deformation and slip along a bounding shear zone; or did it involve chiefly coaxial deformation associated with the emplacement of symmetric gneiss domes? What were the dominant deformation mechanisms (and crystallographic slip systems in quartz) accomplishing this exhumation? Given that dislocation creep and grain-boundary migration recrystallization (GBM) in quartz cannot easily be simulated experimentally at the natural high-temperature conditions appropriate for these rocks [e.g., *Stipp & Tullis*, 2003;
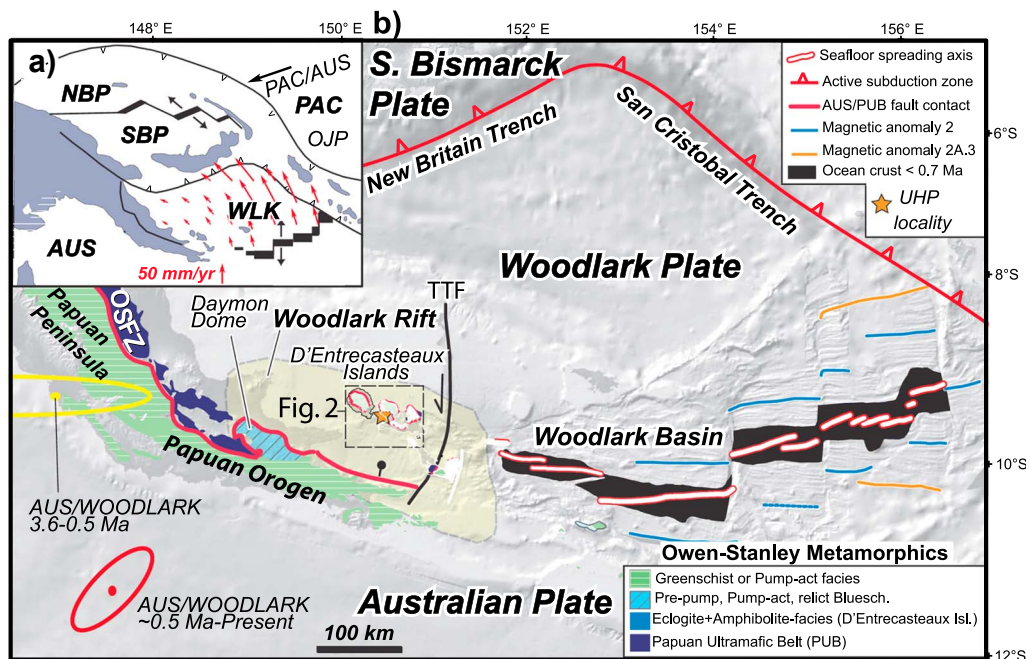
Figure 1. a) Contemporary plate tectonic map of eastern Papua New Guinea: NBP, North Bismark Plate, SBP, South Bismark Plate, WLK, Woodlark Plate, AUS, Australian Plate, PAC, Pacific Plate; OJP, Ontong-Java Plateau. Bold black arrow is contemporary velocity of the Pacific Plate relative to the Australian. Small red arrows depict contemporary velocities of the Woodlark Plate relative to the Australian Plate [after *Wallace et al.*, 2004]; b) Simplified tectonic map of south-eastern Papua New Guinea [modified after *Webb et al.*, 2008; *Little et al.*, 2011], showing key tectonic features and distribution of metamorphic rocks. Background is shaded Digital Elevation Model from GeoMapApp (http://www.GeoMapApp.org). Metamorphic units are simplified from *Davies* [1980] and *Daczko et al.* [2009]. Magnetic anomalies and pole of WLK-AUS rotation for 3.6–0.5 Ma (with error ellipse) is from *Taylor et al.* [1999]; GPS-derived pole of present-day WLK-AUS rotation is from *Wallace et al.* [2004]. Explanation: OSFZ, Owen Stanley fault zone; TTF, Trobriand Transfer Fault.

Heilbronner and Tullis, 2006; *Stipp et al.*, 2010], what can the rapidly quenched, natural microstructures in the D'Entrecasteaux Islands tell us about deformation processes operating at near-solidus temperatures?

[5] Toward these ends, we have analyzed the deformational microstructures and quartz LPOs from 37 samples of strongly deformed quartzofeldspathic gneiss and foliation-parallel quartz veins. The metamorphic tectonites were collected from all exposed levels of all five gneiss domes in the NW D'Entrecasteaux Islands, including the one site with coesite-bearing eclogite. We analyzed the samples using optical microscopy and electron-backscatter diffraction (EBSD). The analyzed rocks span a wide range in both quartz content (11 to 99%) and leucosome fraction (0 to 100%). Our data include EBSD-derived grain maps (e.g., phase maps and Euler-angle maps), pole diagrams and other measures of LPO, and grain-shape fabric (GSF) analyses in quartz.

2. Tectonic Setting

[6] The Pacific and Australian Plates obliquely converge at ~110 mm/yr near eastern PNG [*Wallace et al.*, 2004] across a mosaic of microplates (Figure 1a). The Woodlark Rift is an extending domain of mostly submerged continental crust between the Woodlark microplate, to the north, and the Australian Plate, to the south. This rift transitions eastward into the oceanic Woodlark Basin. The D'Entrecasteaux Islands lie 30–150 km west of the end of that basin's west-propagating spreading ridge (Figure 1b). GPS geodesy indicates that the rift is extending at ~20 mm/yr in a NNW–SSE direction (Figure 1a) [*Wallace et al.*, 2004]. Seafloor-spreading data in the Woodlark Basin indicate that the rift to the west has probably accommodated ~90 km of crustal extension since 3.6 Ma [*Taylor et al.*, 1999]. The seafloor data also indicate that extension occurred in a more nearly N–S direction at 26 mm/yr from 3.6 to 0.5 Ma [*Goodliffe*

et al., 1997; *Taylor et al.*, 1999]. The relatively flat morphology of the 20–30 km-deep Moho of the rift relative to its less stretched flanks [*Abers et al.*, 2002] provides evidence that the rift is underlain by a weak lower crust that has flowed inward away from those rift flanks [*Taylor and Huchon*, 2002; *Westaway*, 2005; *Little et al.*, 2007].

[7] The Papuan Orogen formed as a result of Paleogene collision between the Australian continental margin and an island arc (Inner Melanesian arc) to the NE [*Davies and Jaques*, 1984; *Van Ufford and Cloos*, 2005; *Davies*, 2012; *Baldwin et al.*, 2012]. This orogen occupies the mountainous Papuan Peninsula on the mainland of PNG, as well as the now mostly submerged Woodlark Rift farther to the north. By 58 Ma [*Lus et al.*, 2004], the basement of the arc, the PUB, was emplaced southwestward along the Owen Stanley fault zone (OSFZ) over an orogenic wedge. The mostly Cretaceous wedge sediments are called the Owen Stanley metamorphics. These were scraped off the northern continental margin of the Australian Plate, and emplaced against the upper plate of the orogen (Figure 1b) [*Davies*, 1980; *Davies and Jaques*, 1984; *Hall*, 2002; *Davies*, 2012]. The collision had apparently ceased on the mainland by 35–30 Ma [*Worthing and Crawford*, 1996]. At this time, the paleotrench was filled by >7 km of undeformed orogenic sediment, and much of the orogenic belt had begun to subside below sea level [*Smith and Davies*, 1976; *Rogerson et al.*, 1987; *Van Ufford and Cloos*, 2005]. Some have interpreted a drilled unconformity in the Woodlark Rift as indicating that seafloor uplift and continental rifting began at ~8.4 Ma [*Taylor and Huchon*, 2002]. Oceanic seafloor being subducted at the San Cristobal Trench indicates that seafloor spreading had begun in the Woodlark Basin by ~6 Ma [*Taylor and Huchon*, 2002]. By ~3 Ma, the D'Entrecasteaux gneiss domes had risen above sea level, shedding conglomerate into adjacent marine basins [*Francis et al.*, 1987; *Robertson et al.*, 2001].

3. D'Entrecasteaux Islands Gneiss Domes

[8] The domes of the D'Entrecasteaux Islands (Figure 2) rise to peaks at 2–2.5 km elevation and are remarkable for their geomorphic youthfulness and the rapidity with which the eclogites they contain reached the surface. Two models for the domes have been proposed. The first interprets the domes as detachment-controlled metamorphic core complexes, and infers that the very young eclogites in their footwalls have been exhumed as a result of prolonged slip on mantle-penetrating shear zones and related faults [*Hill*, 1994; *Hill et al.*, 1992; *Webb et al.*, 2008]. The second interprets them as strongly deformed bodies that rose through the mantle as diapirs, later to be deformed and emplaced into the crust as gneiss domes; and with final exhumation accomplished by minor erosion and normal faulting [*Davies and Warren*, 1988; *Martinez et al.*, 2001; *Ellis et al.*, 2011; *Little et al.*, 2011; *Korchinski et al.*, 2012].

[9] The geology of the domes may be summarized as follows (see Figures 2 and 3). Erosional remnants of the PUB mantle the domes. They are stratigraphically overlain by unmetamorphosed, Late Oligocene or Miocene to Quaternary marine sedimentary and volcanic rocks [*Davies and Warren*, 1988]. The lower plate gneisses lie tectonically beneath this poorly exposed upper plate. The contact between the units represents a profound discontinuity in Neogene metamorphic grade, as all of the lower plate rocks are inferred to have experienced eclogite-facies conditions based on the widespread occurrences of eclogite. In the lower plate, the dominant rock type is quartzofeldspathic gneiss—metamorphosed volcanic rocks or greywacke—and abundant tonalitic to granodioritic orthogneiss. Mafic rocks constitute ~5–10% of the lower plate and occur chiefly as m-scale boudins of eclogite and retrogressed (amphibolitized) eclogite. Most of the host gneisses are migmatites, containing 5–15% in situ leucosomes [*Gordon et al.*, 2012]. The leucosomes are typically deformed into concordance with the dominant foliation, especially in the carapace zones (defined below). About 30% of the terrane consists of intrusive bodies of Pliocene granodiorite, leucogranite and related orthogneiss, including abundant dikes at the <1 m scale and plutons at the 1–10's km scale. The volume of these variably deformed, syntectonic dikes increases from as low as 2% in the carapaces to as much as 70% in the core zones. Detrital zircons, a few as old as late Archean, [*Baldwin and Ireland*, 1995; *Waggoner et al.*, 2008; *Gordon et al.*, 2012] and Hf, Pb, and Sr isotopic data indicate that the gneiss sequence was probably derived from a rifted continental margin of Cretaceous age—the conjugate of which lies on the opposite side of the Coral Sea offshore of NE Queensland, Australia [*Korchinski*, 2011; *Zirakparvar et al.*, 2013].

[10] The structural and metamorphic evolution of the domes is constrained by structural studies, thermobarometry, and geochronology, especially U-Pb dating of zircon. Following *Hill* [1994], we refer to the structurally uppermost ~1–1.5 km of
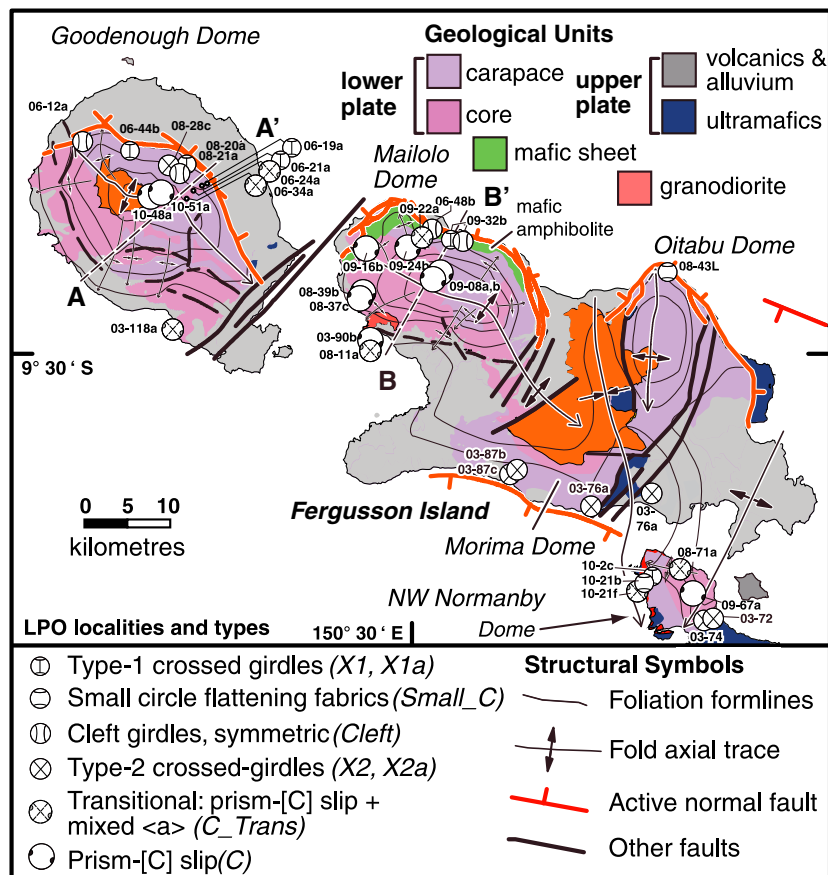
Figure 2. Sample Locations, LPO types. Simplified geological map of the NW D'Entrecasteaux Islands, Papua New Guinea, showing key tectonic features and location of samples that were analyzed for their quartz lattice preferred orientations (LPOs). Map is modified after *Davies*, 1973, *Hill*, 1994 and *Little et al.*, 2011. See text for description of LPO types.

the lower plate, which has a mm-laminated, planar deformational fabric, as the *carapace zone*; and the structurally deeper parts of the domes, which have a cm to dm-banded LS-tectonite fabric, as the *core zone*. In all the domes, both zones experienced a history of eclogite-facies metamorphism followed by widespread upper amphibolite-facies retrogression [*Hill and Baldwin*, 1993; *Hill*, 1994]. Most of the LS-tectonites formed with a flat-lying fabric during the retrogression and were broadly coeval with partial melting and granitoid intrusion [*Hill*, 1994; *Little et al.*, 2011]. The domes are internally homogeneous and no metamorphic isograds for either the eclogite-facies or the amphibolite-facies retrogression are recognized. Evidence for eclogite-facies crystallization is preserved in widespread mafic boudins at all structural levels. In these, equant omphacite and garnet suggest only minor deformation at eclogite-facies conditions. On western Fergusson Island, zircon growth in a coesite-bearing eclogite [T ≥650 °C, P ≥ 27 kbar, *Baldwin et al.*, 2008] has been dated at ~5 Ma [combined TIMS, and ICP-MS

U-Pb methods, also Rb/Sr *Gordon et al.*, 2012], and other U-Pb SIMS dating of zircon in the same rock yielded ages of up to ~7 Ma. HP eclogites (T ≥850 °C, P 20–24 kb) elsewhere on that island have yielded U-Pb ages on metamorphic zircon of 4.3 ± 0.4 Ma [in situ ion microprobe on zircon, *Baldwin et al.*, 2008]. Igneous zircons in the leucosomes and granitoid dikes and plutons on Fergusson and Goodenough Islands have everywhere yielded Pliocene U-Pb crystallization ages. TIMS dating of zircon in a range of strongly to weakly deformed granitoid dikes at several localities indicate that dike intrusion and the bulk of the amphibolite-facies ductile deformation took place in the lower crust at circa 3.5–2.5 Ma [*Gordon et al.*, 2012].

[11] Previous workers have argued that this amphibolite-facies deformation followed rapid ascent of a diapiric eclogite-bearing body from mantle to crustal depths [*Little et al.*, 2011]. If so, little structural evidence of this early phase of rapid
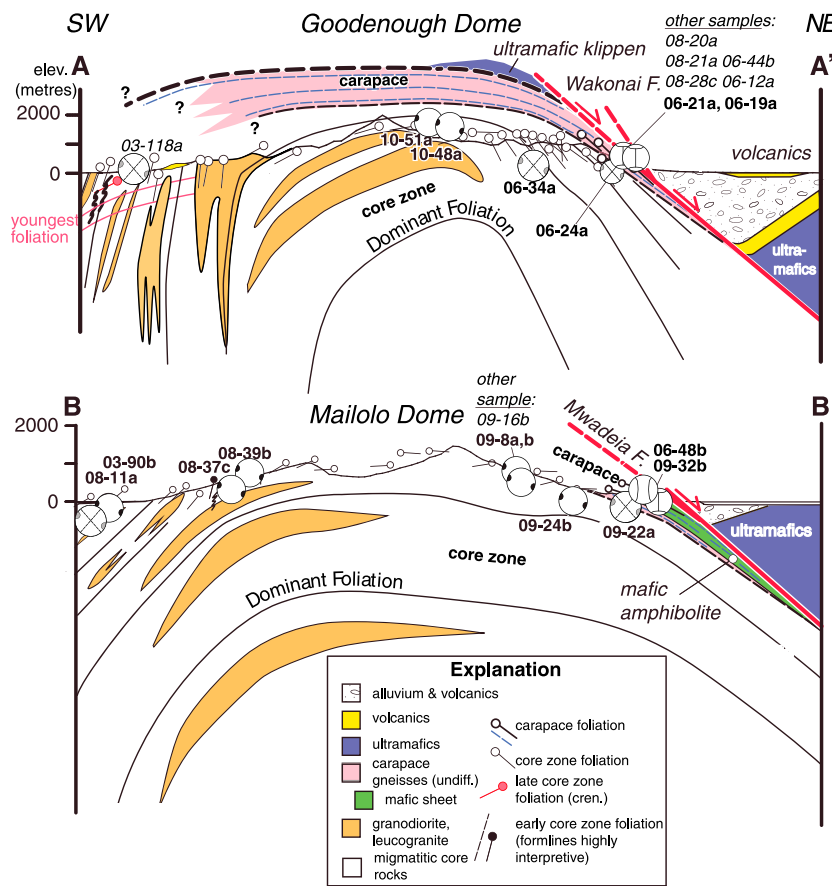
Figure 3. Simplified cross-sections (no vertical exaggeration) across Goodenough (A-A') and Mailolo (B-B') gneiss domes, showing location of LPO samples as projected parallel to foliation strike. Samples that occur <2 km from the section lines are depicted with heavy symbols (same as used in Figure 2), and are labeled with bold font. Samples more distant than 2 km from the section lines are identified at their approximate structural position with italic font. Figure is modified from *Little et al.* [2011].

exhumation remains because of the intensity of the subsequent retrogression at temperatures of 570–730 °C and pressures of 11–14 kb [*Hill and Baldwin*, 1993; *Korchinski*, 2011]. During the overprint, the terrane ductilely thinned and spread outward. By ~2 Ma, the (U)HP terrane had been emplaced as gneiss domes into the upper crust. Final exhumation was by rift-related normal faulting and minor erosion [*Little et al.*, 2011]. Today, active normal faults bound the domes, mostly on their NE sides. Kilometers of slip on these ~30–35° dipping faults have back-tilted the domes by ~20° to the SW [*Little et al.*, 2011].

4. Optical Microstructures

[12] We cut thin sections cut parallel to mineral lineation and perpendicular to foliation. In addition, many of the samples were additionally cut perpendicular to lineation and perpendicular to foliation to produce a second thin section.

4.1. Quartz

[13] Most quartzofeldspathic gneisses in both the core and carapace zones of the domes contain completely recrystallized, irregularly shaped quartz grains. In 2-D section, the grains are up to 200 µm in diameter, but vary widely in shape and size. Quartz-quartz grain boundaries are interlobate (Figures 4a and 4b). In the core zones, grains with amoeboid grain boundaries commonly enclose other smaller isolated quartz grains (island grains, e.g., Figure 4a), presumably because of GBM out of the section plane; or they may be deeply indented by other narrow quartz grains (dissection microstructure, Figure 4b) [*Urai et al.*, 1986]. The amoeboid quartz-quartz grain boundaries have a tendency to form ~90° angles (reticular grains, Figure 4a) [described by *Lister and Dornsiepen*, 1982; and *Pennacchioni et al.*, 2010]. Deformed quartz layers or veins tend to be inequigranular in 2-D section, containing a few unusually coarse grains up to several mm in diameter (e.g., Figure 4a).
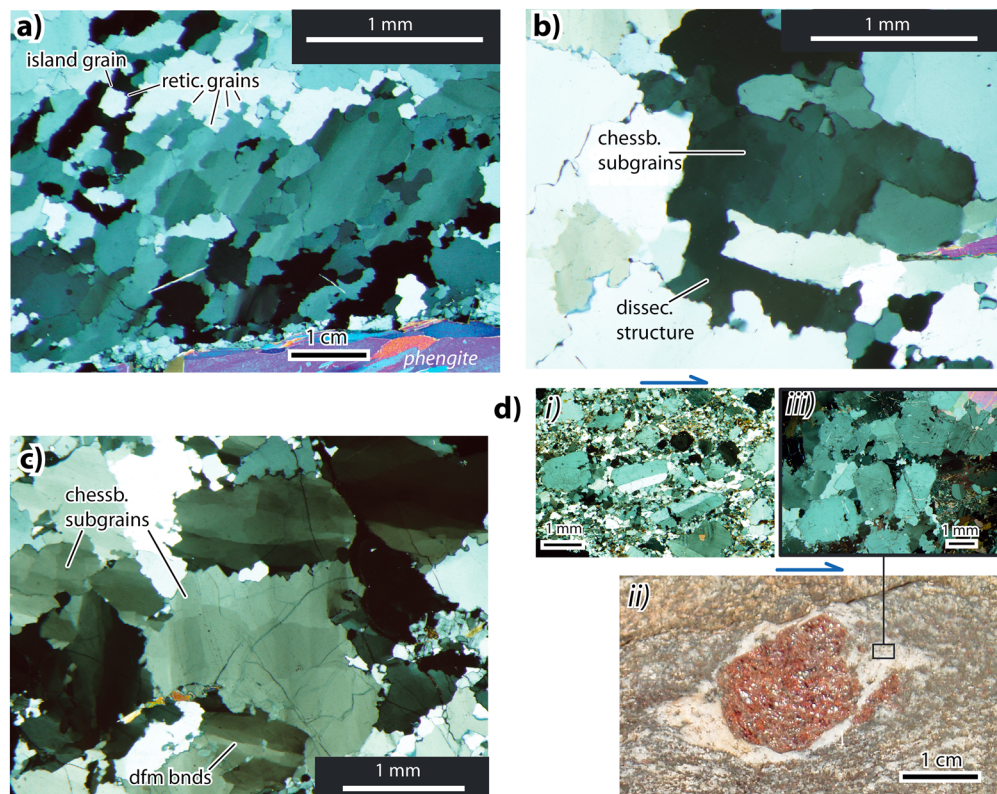
Figure 4. Optical photomicrographs of quartz microstructures. All photographs were taken under crossed polarized light in lineation-parallel (XZ) thin sections. Foliation trace is horizontal. a) Deformed phengite-bearing quartz vein (core zone) at UHP eclogite locality offshore of Fergusson Island (sample PNG-08-011a), showing high-temperature GBM microstructures in quartz, including amoeboid (also reticular) grain boundary structures, island grains, and dissection microstructures; b) deformed quartz vein (core zone) from NW Fergusson Island (sample PNG-08-039a) showing dissection structure and chessboard patterns; c) deformation bands and chessboard sub-grain pattern in quartz in deformed pegmatite dike at UHP locality (core zone) offshore of Fergusson Island (sample PNG-08-010d); d) selected evidence for melt-present deformation (blue arrows show sense of shear): i. photomicrograph leucosome (partial melt phase) infilling a ductile shear zone on Goodenough Island (core zone, PNG-06-035A) showing rotated and tiled igneous feldspar crystals; ii, outcrop photograph of a garnet strain shadow (carapace zone, Goodenough Island, PNG-06-020) that has been infilled with leucosome; iii, inset shows photomicrograph of part of the strain shadow (note euhedral igneous feldspar crystals).

[14] Quartz grains in the gneisses contain sweeping undulose extinction and/or deformation bands (Figures 4a and 4c). The most common crystallographic orientation for deformation bands is prismatic, $\{10\bar{1}0\}$, but an additional set of basal (0001) deformation bands occurs in some grains. This relationship is most obvious in quartz aggregates that have an LPO featuring a single strong [c]-axis maximum in the XZ plane (see below). In some (but not all) of the grains, both sets of deformation bands occur inside individual quartz grains to define a chessboard pattern (Figures 4b and 4c).

4.2. Feldspar and Mica

[15] The D'Entrecasteaux Islands gneiss domes consist predominantly of one- or two-mica bearing quartzofeldspathic gneisses. In the gneisses, recrystallized plagioclase (and porphyroclast rims) is generally An_{20-30} oligoclase, [*Hill and Baldwin*, 1993; *Korchinski*, 2011]. Most plagioclase porphyroclasts are antiperthitic, whereas K-feldspar porphyroclasts are perthitic (Figures 5a and 5c). In the gneisses and in deformed dikes, feldspar grains are inequigranular, ranging from $<100\,\mu m$ in the recrystallized matrix to several mm in relict porphyroclasts. Many of the coarser ($>300\,\mu m$) plagioclase and K-feldspar grains in both the core and carapace zones have approximately rhombic cross-sections (Figure 5a). Their boundaries are finely to coarsely lobate, and indentations occur where quartz grains abut the feldspar (white arrows in Figures 5a, 5b, 5c, and 5d). Impingement of quartz into the feldspar produced a cuspate-lobate morphology with the cusps pointing away from the feldspar. Feldspar-feldspar grain contacts are nearly planar.
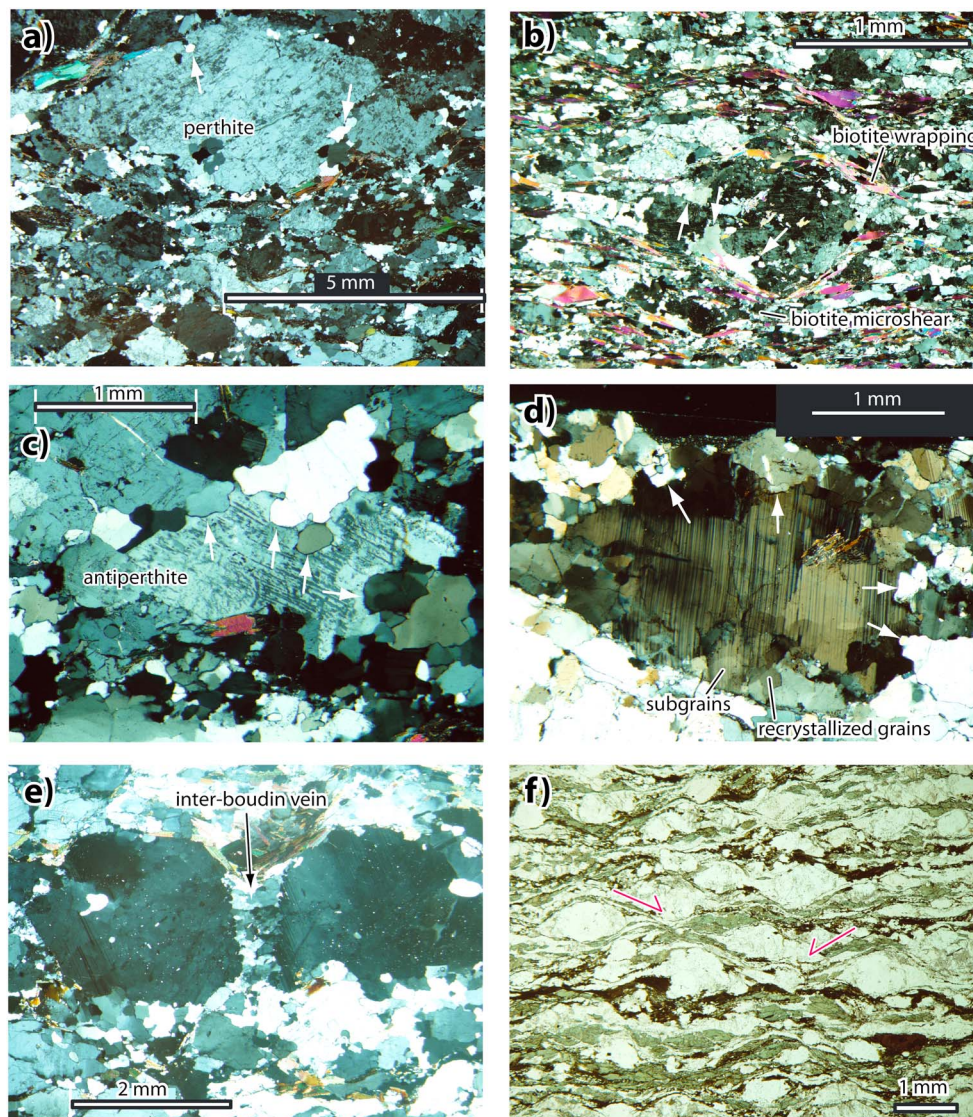
Figure 5. Optical photomicrographs of feldspar microstructures. All photographs were taken under crossed polarized light in lineation-parallel (XZ) thin sections. Foliation trace is horizontal. a) deformed granitic sheet, Goodenough Island (core zone), showing mosaic of rhombic shaped, mesoperthitic K-feldspar grains defining foliation-parallel SPO. The feldspars have crenulate margins that are indented against quartz grains (white arrows, sample PNG-10-058a); b) deformed pegmatite, Mailolo dome (carapace), showing rhombic-shaped plagioclase porphyroclast that is wrapped by biotite folia (one of which extends as a shear band into the matrix) and deeply indented by quartz grains (white arrows). Strain shadows consist of quartz, feldspar, and biotite (sample PNG-08-018c); c) foliation-parallel antiperthite (plagioclase) grain from quartzofeldspathic gneiss (core zone) in the Mailolo dome, showing scalloped phase boundary against quartz grains (white arrows, sample PNG-09-025b); d) plagioclase porphyroclast in deformed granodioritic orthogneiss at UHP locality (core zone) offshore of Fergusson Island, showing evidence for both plastic deformation (e.g., undulose extinction) and recrystallization by SGR (subgrains, recrystallized grains), and localized dissolution and grain boundary migration. White arrows point to phase boundary embayments in plagioclase against quartz (sample PNG-08-010c); e) microboudinaged plagioclase porphyroclast from granodioritic orthogneiss (carapace zone), Goodenough Island. The inter-boudin dilation space is infilled with fine-grained K-feldspar (sample PNG-06-012a); f) conjugate extensional shear bands in hornblende-bearing quartzofeldspathic gneiss (sample PNG-08-049c) from Oitabu Dome (carapace zone).

[16] The interiors of plagioclase porphyroclasts are either undeformed or include one or more of the following microstructures: undulose extinction (Figure 5d); tapered deformation twins; microkinks of lamellar twins; fractures along cleavage (most common in carapace rocks); subgrains (polygonization near porphyroclast margins, Figure 5d); and, more rarely, deformation bands and/or seams

of recrystallized grains, especially in deformed pegmatites. There is a tendency for (010) planes (albite twins) in porphyroclasts to be aligned either parallel or perpendicular to the foliation (e.g., Figure 5d) [see also *Kruse et al.*, 2001]. K-feldspar microstructures include fractures, undulose extinction, subgrains and myrmekite. Undeformed recrystallized feldspar grains, similar in size to subgrains, are occasionally recognizable adjacent to porphyroclasts, and we infer that these probably formed as a result of subgrain-rotation recrystallization (Figure 5d). Obvious core-and-mantle textures are uncommon. Any mantles of recrystallized feldspar grains that may once have enveloped porphyroclasts of feldspar are now difficult to distinguish from the surrounding polymineralic matrix. The long dimensions of porphyroclastic feldspar rhombs are aligned parallel to the foliation. In almost all samples, coarse plagioclase and K-feldspar grains (also quartz aggregates) are more elongate in XZ sections (Figures 6a and 6c) than they are in than in YZ sections (Figures 6b and 6d).

[17] Feldspar porphyroclasts are set in a matrix of feldspar, quartz, and mica with a typical grain size of ~200–300 m (e.g., Figure 5b). Feldspars in this matrix are equant to elongate, typically lack exsolution sub-structures, and have straight to lobate boundaries. Finally, feldspar (most commonly K-feldspar) occupies strain shadows adjacent to feldspar porphyroclasts (Figure 5b) and infills the necks between feldspar microboudins (Figure 5e).

[18] Asymmetric mica fish (mostly white mica) are common in the carapaces [*Little et al.*, 2011]. The fish are mostly C'-parallel, but in some samples (e.g., Appendix C, sample 03-087b) they are lenticular fish in a C arrangement [classification of *ten Grotenhuis et al.*, 2003]. Elsewhere, mica grains (mostly biotite) are concentrated in elongate seams subparallel to the foliation. These wrap the rhombic feldspar grains symmetrically with respect to the foliation (Figures 6c and 6d) and may have conjugate-sense extensional shear displacements (Figure 5b).

5. Measuring Quartz Lattice Preferred Orientations (LPOs)

[19] Quartz crystallographic orientations were measured in 37 samples of quartzofeldspathic gneiss and deformed, foliation-parallel quartz veins (Figure 2 and Table A in the auxiliary material).[1]Appendix A

_____
[1]Additional supporting information may be found in the online version of this article.

describes our sample preparation methods, and the techniques we used to measure, process, and present LPO data using EBSD. Appendix B describes the mineralogy and microstructure of each sample in detail. Collected at diverse structural levels across all five of the eclogite-bearing gneiss domes of the NW D'Entrecasteaux Islands, the samples all contain the same syn-exhumational, amphibolite-facies foliation, and stretching lineation. This dominant fabric was later warped to form the currently exposed gneiss domes [*Little et al.*, 2011]. Because all the samples share a common (originally flat-lying) foliation of regional extent that formed during the retrogressive metamorphism, the broad structural context of all the samples is comparable, with the chief differences being between the carapace and core-zone samples (the former have a stronger and more laminated fabric, as described above). Microstructural and lithological variations among different quartzofeldspathic gneiss samples are small, and sample-specific compositional differences do not have an obvious impact on the resultant quartz LPO patterns (e.g., in fraction of mica, as discussed below).

[20] Quartz crystallographic orientations were measured in 33 samples by EBSD. Prior to our undertaking the EBSD analyses, an additional five samples were analyzed as part of a pilot study with a Leitz 4-axis Universal stage to obtain [c]-axis pole figures from an analysis of 300–400 quartz grains. One sample (03-087b, c) was analyzed by both U-stage and EBSD methods, yielding comparable [c]-axis LPOs (see Appendix C, data for Morima dome). EBSD-derived Euler angle maps, and detailed sample location data are provided for each sample in Appendix B. Lower hemisphere, equal-area pole figures, were created and contoured by the program *PFch5* [*Mainprice*, 2005]. For each sample, the following crystallographic directions and planes were plotted in the rock fabric (XYZ) reference frame: $[0001]$ (c axes); $<2\bar{1}10>$ (a axes, collapsed using 622 symmetry); $\{10\bar{1}0\}$ (m, prism planes); $\{10\bar{1}1\}$ (r rhomb planes); and $\{01\bar{1}1\}$ (z rhomb planes). The LPO fabric strength was measured in two ways: (1) using the J index [*Bunge*, 1977] for the [c]-axis fabrics (only); and (2) using the M index, which accounts for the full 3D crystallographic misorientations among all grains [*Skemer et al.*, 2005]. We estimated the modal proportion of quartz in each sample based on the fraction of such grains that were indexed during the EBSD scans. This fraction is precise to within ±5%. LPO fabric strengths and modal abundances of quartz are presented in Table A.
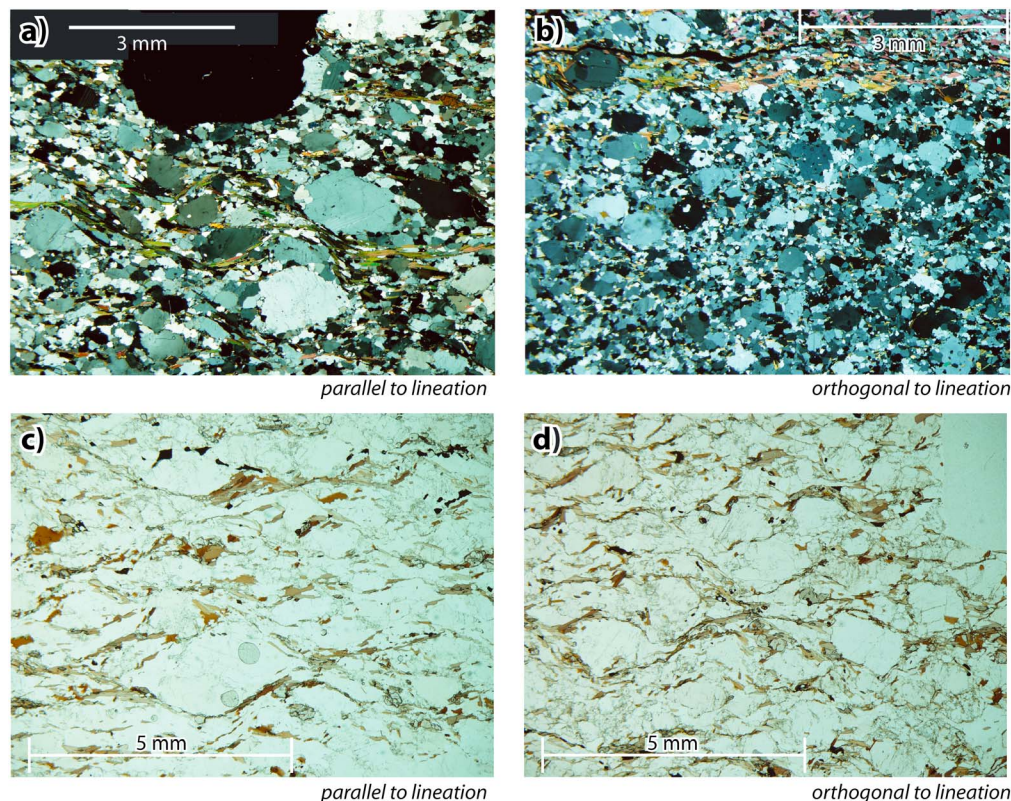
Figure 6. Optical photomicrographs comparing the Shape Preferred Orientation (SPO) fabrics of thin sections that are parallel (left-hand side) and perpendicular to lineation (right-hand side). Foliation trace is horizontal. a) and b) photomicrographs of mica-poor quartzofeldspathic gneiss from Goodenough Island (carapace zone), taken under crossed polarized light (sample PNG-06-10a); c) and d) photomicrographs of biotite-rich quartzofeldspathic gneiss from Goodenough Island (carapace zone), taken under plane polarized light (sample PNG-06-11a). Note the rhombic shaped-feldspar porphyroclasts wrapped by biotite films that have undergone shearing in conjugate senses; and the stronger shape-preferred orientation of feldspar grains in lineation-parallel sections relative to lineation-perpendicular ones.

[21] Measures of quartz grain shape in 2D as observed on XZ planes were compiled from the EBSD data in the Grain Detection module of the program, "Tango" in HKL Channel 5, which fits ellipses to each crystallographically defined grain. We used a minimum misorientation angle of 10° to define a quartz-quartz grain boundary, and analyzed all detected grains that had a mean of diameter of at least four times the grid spacing (which varied between 5 and 20 microns for different samples). Rose diagrams of quartz grain ellipse orientations were also plotted for each sample using the program Georient (v.9) [*Holcombe*, 2008] (Figure 7e).

6. Thermobarometric Constraints

[22] The published thermobarometric data relating to the amphibolite-facies deformation are imprecise [*Davies and Warren*, 1988; *Hill and Baldwin*, 1993]. Previous temperature and pressure estimates by these authors based on conventional thermobarometry are in the range of 570 – 740 °C, and 7 – 11 kbar,

respectively. More recently, *Korchinski* [2011] and *Korchinski et al.* [manuscript in review] used Zr-in-Rutile thermometry to estimate peak temperatures of 700 ±30° in a kyanite-bearing sample of pelitic core-zone rocks and 625 ± 30° in a pelitic sample of carapace-zone rocks. Combining these temperatures with garnet-aluminosilicate-plagioclase barometry led them to estimate syn-retrogression pressures of 14 ±2 kb and 12.5 ±2 kb, respectively [*Korchinski et al.*, manuscript in review]. We emphasize, however, that LPOs measured in these rapidly exhumed, migmatitic rocks cannot easily be attributed to a specific "point" in the PT history as they may have developed during ongoing syn-exhumational deformation that took place after the peak of amphibolite-facies mineral growth.

7. Microstructures on EBSD Maps

[23] Some microstructures are more obvious in EBSD phase and crystallographic orientation maps
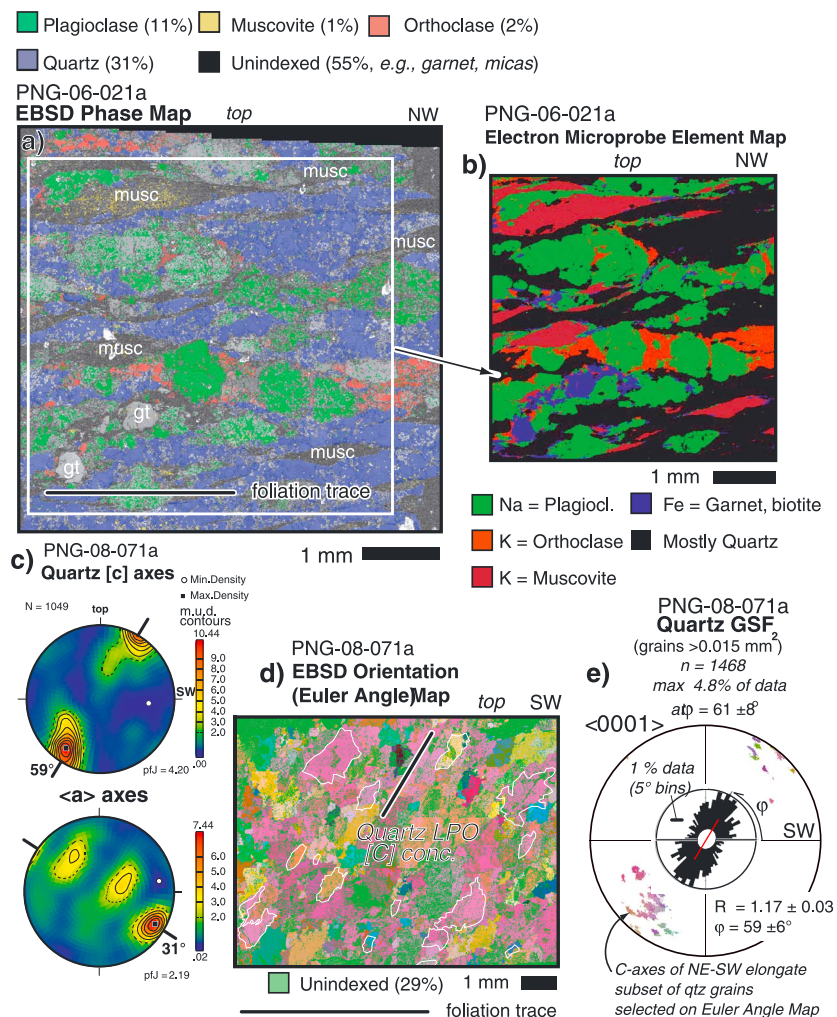
Figure 7. Selected EBSD Maps. a) Phase map of sample png-06-021a (Goodenough dome, carapace) mapped at 10 m grid spacing and overlain on band contrast grayscale image (note muscovite does not index well). b) Electron microprobe element map of part of the same sample. Note the occurrence of K-feldspar in dilatational sites between plagioclase grains or grain fragments. c) Lower hemisphere quartz [c] axis pole figure of sample 08-071a from NW Normanby dome (core zone) showing peripheral maximum of [c] axes; d) corresponding EBSD orientation maps showing high-angle-to foliation oblique grain-shape fabric (GSF) parallel to the [c] maximum, highlighting selected grains with this GSF orientation; the map is color coded by Euler angle, with changes in color indicating crystallographic orientation differences (these angles are difficult to interpret visually, so a look-up table is not included); e) (larger) pole figure shows [c] axis orientations of the highlighted grains selected in d), color coded by Euler angle (using same color scheme as the EBSD map. Inner circle is rose diagram of grain elongation directions (5° bins) as interpreted by the Grain Detection module of HKL Channel 5. R is mean fabric axial ratio (±1) of the detected grains (n = 1468). is mean angle of the grain shape fabric long axis direction relative to foliation.

than with an optical microscope. On some phase maps, for example, microveins of fine-grained, neocrystallized K-feldspar filling of cracks in feldspar porphyroclasts and strain shadows are especially evident (e.g., Figures 7a and 7b; also in Appendix B, data for samples 06-012a, 06-019a, and 06-024a). A second is the well-dispersed nature of the fine-grained (100–200 m diameter) quartz+plagioclase ± K-feldspar matrix (Appendix B, samples 06-019a, 06-040a, 06-044b, 06-048b, 10-021f). Finally, the EBSD

phase maps show that quartz grains become increasingly interconnected (at least in the XZ plane) at quartz fractions of >30%, resulting n the development of foliation-parallel quartzose lenses that have an X:Z aspect ratio of >5:1 (e.g., Figure 7a). Of the nine samples containing <30% of quartz, eight of them yielded EBSD phase maps in which the quartz occurs chiefly as isolated grains or small aggregates that are separated by the other, more abundant phases (chiefly feldspar).

8. Quartz LPOs as a Function of Structural Depth Into the Domes

[24] All five of the D'Entrecasteaux domes yielded a similar progression of LPOs from the carapace zone structurally downward into the core. Our sample localities are plotted on Figures 2 and 3, whereas our classification of LPOs into six reference types is defined in Table 1. Below, we describe these LPO types from structurally highest to structurally deepest and present representative pole diagrams for them in Figure 8. Appendix C presents the complete set of pole figures arranged by dome and structural position. Synoptic fabric skeletons for each LPO type were compiled by drawing the fabric skeletons and/or orientation modes (areas of greatest orientation density) for each sample and superimposing these onto a single pole figure (Figure 9).

8.1. Small Circle LPOs (Small_C)

[25] Two samples of gneiss from the structurally highest parts of the carapace zone yielded symmetrical small circle distributions of both [c] and $<a>$ axes about the Z fabric direction (e.g., Figure 8a). The [c]-axis small-circle girdles are located ~30° from Z, with corresponding $<a>$ axis girdles at ~60–70° from Z (Figures 8a and 9a). The (r)-rhomb poles define a girdle in the XY plane and include a maximum near Z (Figure 8a, also Appendix C, sample, 10-021b).

8.2. Type-1 Crossed Girdle LPOs (X1)

[26] Five samples of gneiss, all from the carapace zone, yielded type-1 crossed girdles of [c] axes [*Lister*, 1977; *Schmid & Casey*, 1986; *Law*, 1990]. These crossed girdles are typically weak or incomplete. The patterns include small circles of [c] axes about Z and/or a maximum in the XZ plane at a small angle to Z. The central limb of the crossed girdles is represented by maxima of [c] axes in the YZ plane, and in some cases by a concentration parallel to Y (Figures 8b, 8c, and 8d; Figure 9b). The same LPOs are characterized by conjugate maxima of $<a>$ axes in the XZ plane. These $a>$ axis maxima are disposed symmetrically about X at angles of 20–30° (Figures 8b, 8c, and 8d; Figure 9b). In most samples, a maximum of {r} rhomb poles occurs near Z, whereas {z} rhomb poles form girdles between Z and Y, and also define a maximum near X. Only one of the five LPOs that we include in this group is obviously asymmetric with respect to the foliation (sample 10-002c,

Appendix C). This sample features an inclined single girdle of [c] axes and incorporates a single maximum of $<a>$ axes in the XZ plane near X rather than a conjugate set as described above. The other four type-1 crossed-girdle LPOs are symmetric with respect to the foliation.

8.3. Cleft Girdle LPOs (Cleft)

[27] Five samples of gneiss, all from the carapace zone, yielded symmetrical cleft girdle (small circle) distributions of both [c] and $<a>$ axes about X (e.g., Figures 8d and 8e). The [c]-axis small circles are at ~65° to X, whereas the $<a>$ axes are at ~35° to X (Figure 9c). In several of these five samples, {r} rhomb plane poles form girdles in the YZ plane and a maximum parallel to X, whereas the {z} rhomb planes are distributed in small circles about X (Figures 8d and 8e; Appendix C, samples 06-012a and 06-048b).

8.4. Type-2 Crossed Girdle LPOs (X2 and X2a)

[28] Seven samples of gneiss from deeper parts of the carapace zone and near the carapace-core transition yielded LPOs that we classify as type-2 crossed girdles [after *Lister*, 1977; Schmid & Casey, 1986; *Law*, 1990; *Law et al.*, 2004]. LPOs in this group are characterized by weak or incomplete crossed girdles of [c] axes intersecting near the Y fabric direction and having an opening angle of ~90° (e.g., Figures 8f, 8g, and 8h). The [c] axes commonly define two orthogonal maxima in the XZ plane (Figures 8g and 9d). Between these two horizontal maxima and Y, one or both of the crossed girdles may be incompletely developed. One of the two samples that we analyzed using EBSD (sample 08-028c, Figure 8f) features twin maxima of $<a>$ in the XZ plane at 30–45° to X that are approximately perpendicular to conjugate [c]-axis maxima on the perimeter of the same sample. This distribution of [c] and $<a>$ axes is consistent with basal-$<a>$ slip (Figure 9d). In addition, a secondary maximum of [c] axes parallel to Y is present in half of the samples (03-074a; 03-076a, 03-082a, 08-028c), which suggests prism-$<a>$ slip. In half of the samples, each of the two [c]-axis maxima (and also $<a>$ axes, where measured) in the XZ plane are of approximately equal strength to define an LPO with an apparent orthorhombic symmetry (X2 sub-type, Figures 8f and 8g), whereas in the other samples, one maximum is stronger than the other (asymmetric X2a subtype, Figure 8h).

Table 1. Description of Quartz LPO Types

LPO Type	Attributes	Interpretation	Active Slip Systems	Samples
Small_C	Small circle pattern Carapace zone only Narrow (~30°) small circles of [c] about fabric Z Wide (60–70°) small circles of $<a>$ about fabric Z Orthorhombic symmetry Transitions to X1	Flattening strain Lower T	$<a>$(001), $<a>$ {r}	n = 2 08-043L 10-021b
X1	Type I crossed girdle Carapace zone only Opening angles <90°; Girdles may be incomplete $<a>$ axes on periphery at acute conjugate angles to fabric X Typically orthorhombic in symmetry, but may be asymmetric (sub-type, X1a) Transitions to cleft and to X2	Plane strain (Pure shear) Lower T	$<a>$(001), $<a>$ {r}, $<a>$ {p}	n = 5 06-019a 06-044b 08-020a 09-032b (X1a) 10-002c
Cleft	Cleft girdle pattern Carapace zone only Wide (60–70°) small circles of [c] about fabric X (± incomplete) Narrow (~30°) small circles of $<a>$ about fabric X Orthorhombic symmetry Transitions to X1	Constrictional strain Lower T	$<a>$(001), $<a>$ {r}, ± $<a>$ {p}	n = 5 06-012a 06-021a 06-048b 08-021a 09-032b
X2	Type 2 crossed girdle Carapace or carapace-core transition only Opening angles ~90° Includes strong peripheral concentration of [c] axes in conjugate sets at acute angles to fabric Z [c] conc. parallel to fabric Y may or may not be present $<a>$ axes on periphery at acute conjugate angles to fabric X (±girdled) Symmetry may be orthorhombic; or one girdle may be stronger and more complete than the other (sub-type, X2a) Transitions to X1 and C_Trans	Plane or constrictional strain Moderate T (Amphibolite facies)	$<a>$(001), $<a>$ {p}, $<a>$ {r}	n = 7 (X2a) 03-072a 03-074a (X2a) 03-076a 03-082a (X2a) 03-087b (X2a) 03-087c 08-028c
C_Trans	Transitional to prism C-slip Core zone, or carapace-core transition Opening angles ≥90° Peripheral concentration of [c] axes may be present that is inclined at small angle to Z, ±extending as a girdle through Y Another [c] concentration occurs on the periphery at a small (<45°) angle to X $<a>$ conc. occurs on the periphery at small angle to fabric X, overlapping with the [c] mode	Plane strain High T (Upper amphibolite facies)	$<a>$(001), $<a>$ {p}, $<a>$ {r}; also [C] {p}	n = 8 03-118a 06-024a 06-034a 06-040a 08-011a

Table 1. (continued)

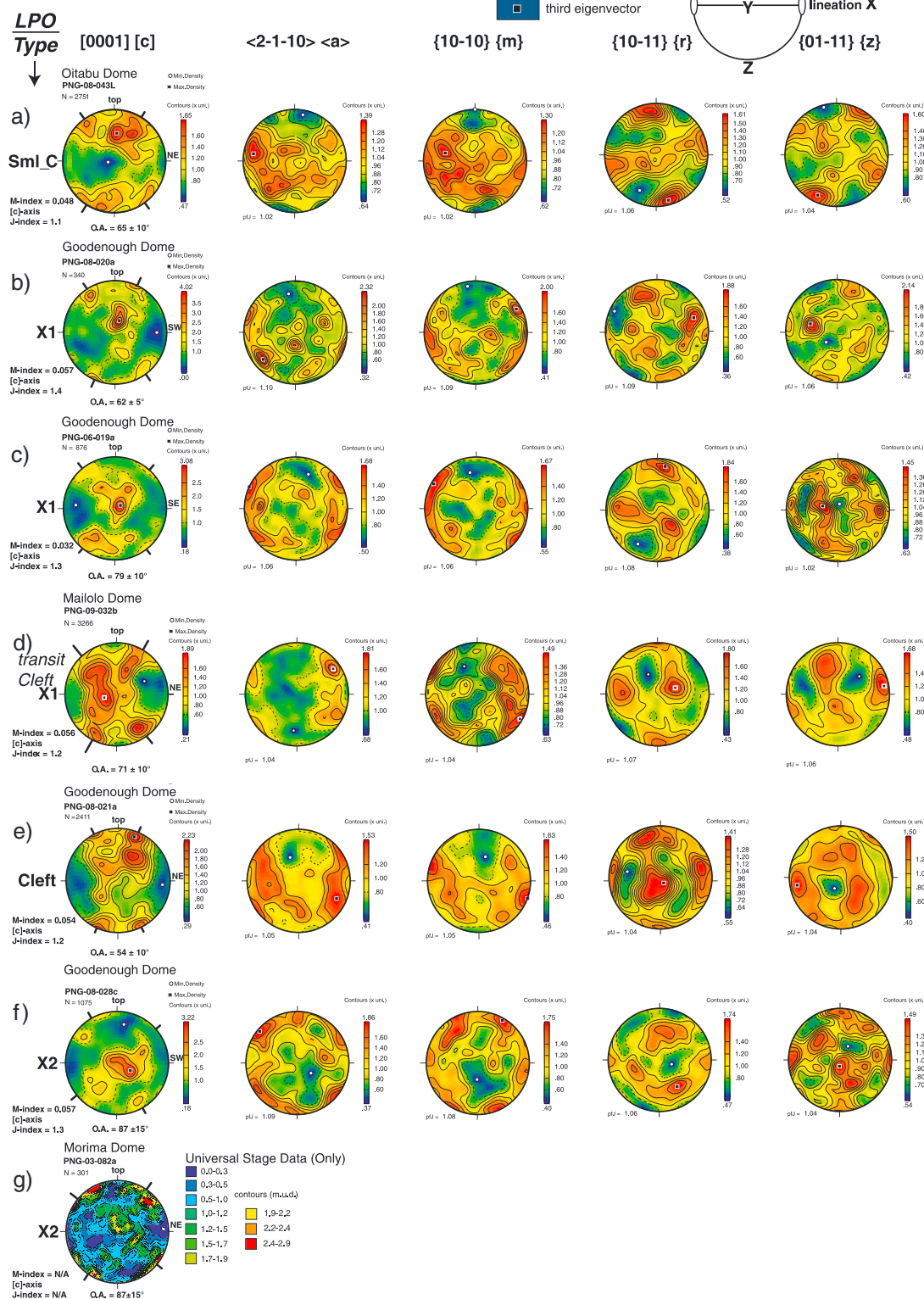| LPO Type	Attributes	Interpretation	Active Slip Systems	Samples
	Commonly a vertical [c] concentration occurs parallel to fabric Y		[C] {p}, ± $<a>$ (001)	08-071a
	Typically asymmetric			09-022a
	Transitions to X2 and C			10-021f
	Prism-[C] slip pattern	Noncoaxial plane strain		n=12
	Core zone only	High T		03-090b
	Opening angles not defined (no girdles)	(Upper amphibolite facies)		06-034a
	Strong [C] concentration on periphery at small angle to fabric X			08-016b
	May be a secondary [C] mode at small angle to fabric Z which is part of an			08-037c
	inclined girdle of c-axes through Y			
	$<a>$ axes often define three modes in girdle around the peripheral [C] concentration			08-039b
	(quasi single-crystal pattern)			
	May be a secondary mode of $<a>$ axes near fabric X			
	{m} poles define three modes in girdle around the peripheral [C] conc.			09-008a
	(quasi single-crystal pattern)			
	One of the {m} modes is typically on periphery, coplanar with the [c] concentration			09-008b (gneiss)
	near Z, or may be girdled			
C	Typically asymmetric			09-008b (leucsm)
	Transitions to C_Trans and basal			09-024b
				09-067b
				10-048a
				10-051a

Figure 8. Representative pole figures of LPOs from gneisses of the D'Entrecasteaux Islands (also deformed quartz veins). Lower hemisphere, equal-area projections. See Table 1 for explanation of the LPO types, indicated by the abbreviations, "Small_C", "X1", "Cleft", "X2", "C_Trans", and "C" at the far left. [C]-axis crossed-girdle opening angles (O. A.) are given below the left-hand pole figure that plots the [0001] axes. These pole diagrams also identify with outer tick marks (and give inclination angle from the foliation plane) of each the peripheral maximum in [c] axes (if any).
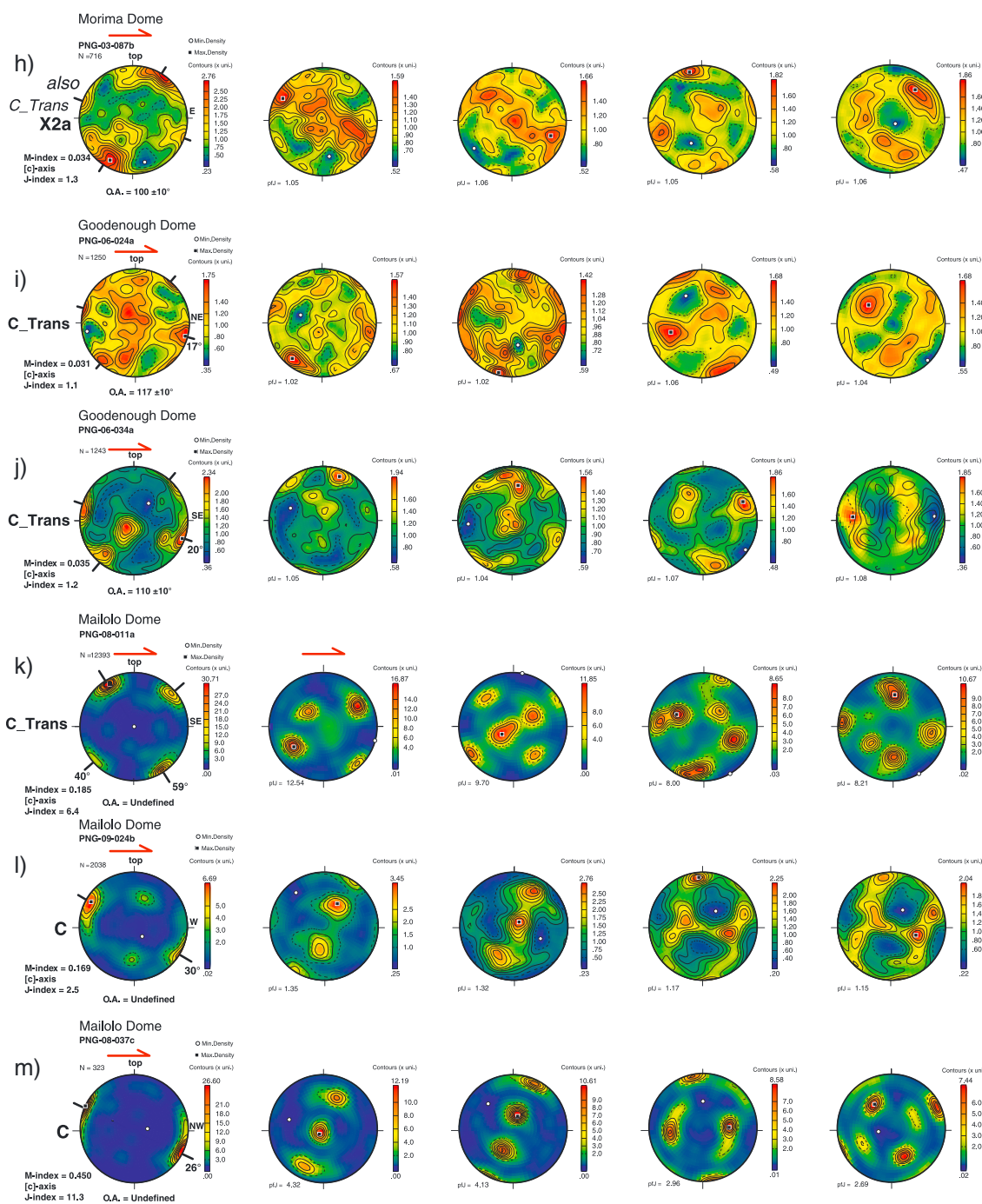
Figure 8. (continued)

8.5. Transitional to [C]-Slip LPOs (C_Trans)

[29] Eight samples (including three quartz veins) from the core-carapace transition and deeper in the core zone contain quartz LPOs that are transitional between the type-2 crossed girdles described above, and the [c]-slip LPOs described below. The samples in this transitional group feature a [c]-axis maximum in the XZ plane at a small (~20–30°) angle to X (Figures 8h, 8i, and 8j), plus a concentration of < a > axes that

overlap with this [c] axis concentration in an approximately co-linear way (Figures 8h, 8i, and 8k). In contrast to the previously discussed LPOs, which are dominantly symmetric with respect to the foliation, the LPOs in this "transitional to [c]-slip" group are mostly asymmetrical (Figure 9e). The asymmetry is defined by: (1) the acute angle between the outer [c] axis maximum and X; and (2)—at right angles to this [c]-axis maximum—the similar acute angle between
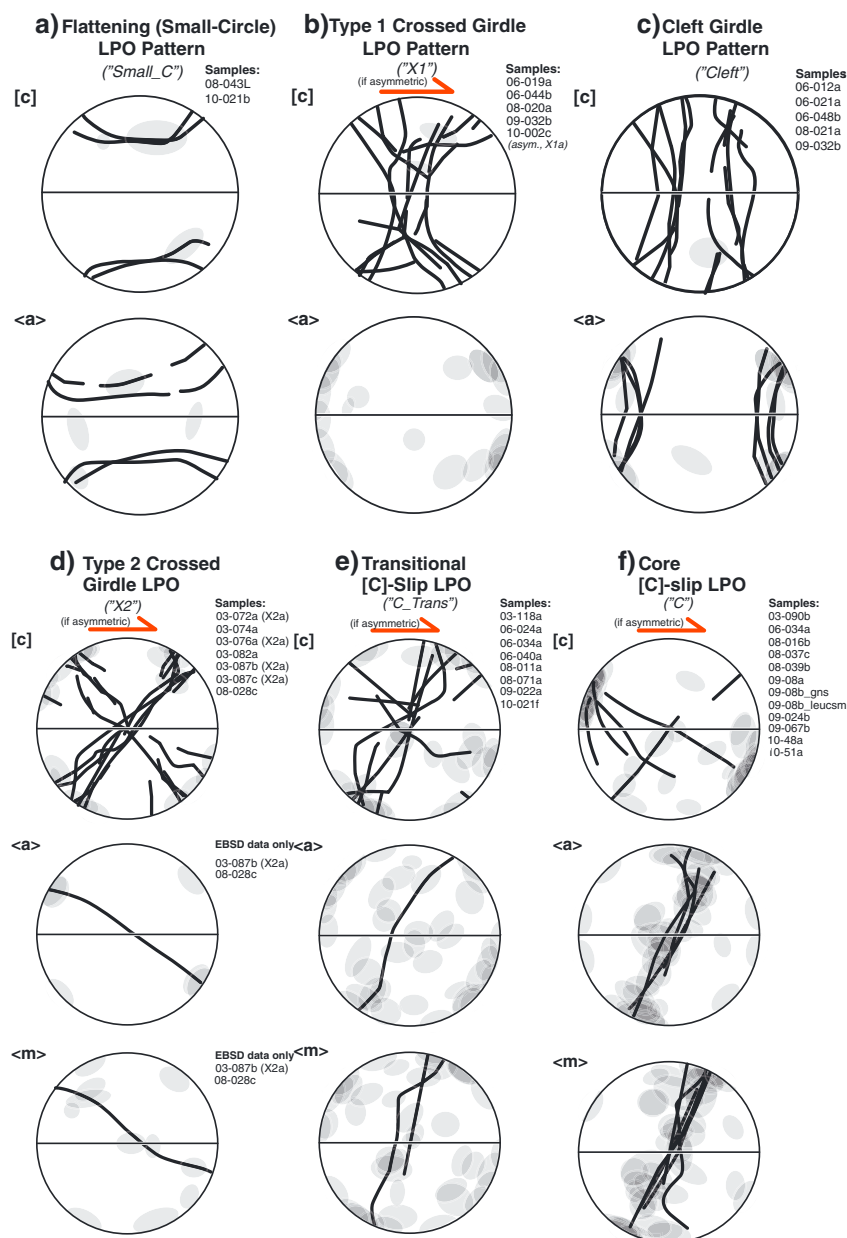
Figure 9. Synoptic pole figures of LPOs from gneisses of the D'Entrecasteaux Islands (also deformed quartz veins). Lower hemisphere, equal-area projections. Each diagram lists the sample numbers that have been grouped with that LPO type, and overlays fabric skeletons (heavy lines) for girdled data) and/or fabric loci (gray ellipses) for distinct maxima. The full pole figures are presented in Appendix C, where they are organized by dome and relative structural depth of the sample. See Table 1 for explanation of the recognized LPO types, which include: a) Small-Circle (Flattening) pattern; b) Type-1 Crossed Girdle; c) Cleft Girdle; d) Type-2 Crossed Girdle; e) Transitional to [C]-Slip LPO; and f) prism-[C]-slip LPO.

vertical [c]-axis girdles and Z. The latter girdles resemble those in a type-2 crossed-girdle LPO. A maximum of prism plane poles (<m> poles) occurs near Z.

8.6. [C]-Slip LPOs (C)

[30] Thirteen samples from the core zones of all the domes have LPOs that include a [c]-axis maximum

in the XZ plane that lies at a small angle to X (Figures 8l, 8m, and 9f). These include six samples of quartzofeldspathic gneiss and seven deformed quartz-rich veins that are approximately concordant to the gneissic foliation. The [c]-axis maxima in these rocks are typically oblique to X by 20–30°, although a few samples display a second, weaker concentration of [c] axes subparallel to X. All of the LPOs
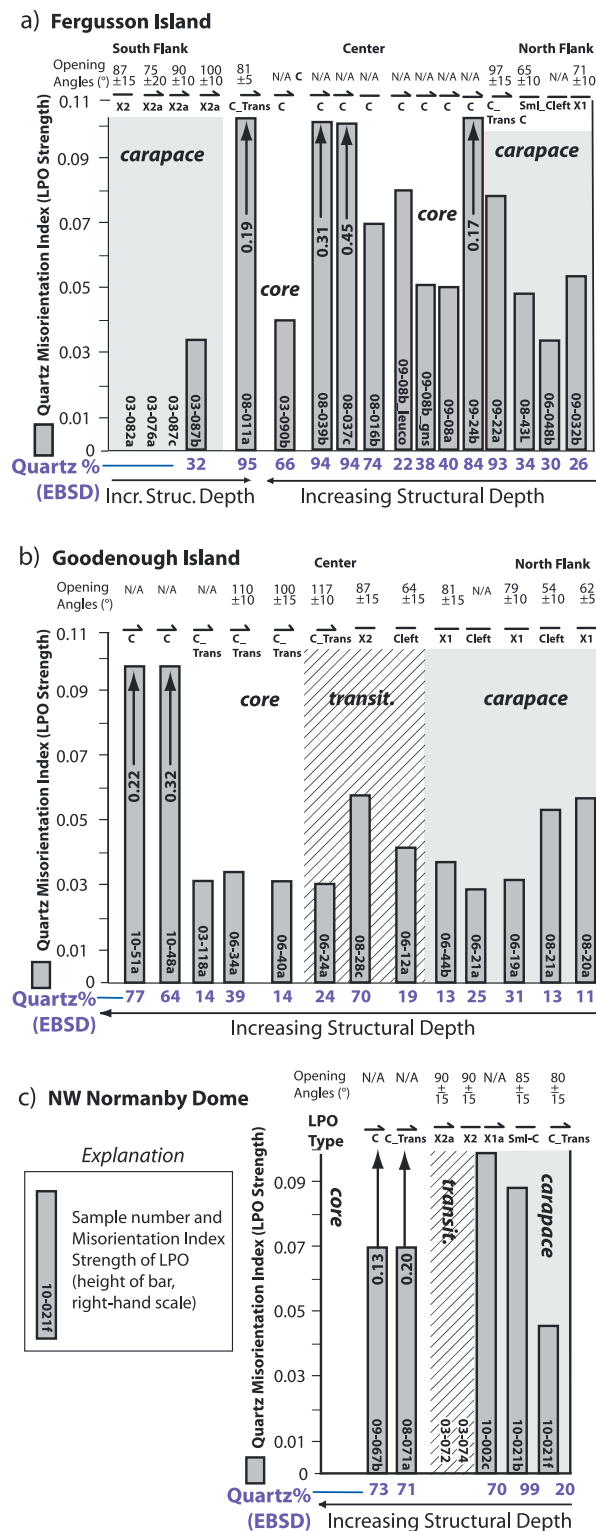
are asymmetric. In contrast to the transitional LPOs, the [c]-slip LPOs generally lack an < a > axis maximum that is co-linear to the [c] axis maximum. Instead, the < a > axes (also the < m > poles) define six maxima perpendicular to the [c] maximum and separated by 60°, approximating a single-crystal LPO. Some quartz-rich veins have very strong LPOs with [c]-axis J values of >20, see below). A maximum of < m > plane poles falls in or near the XZ plane, where it is oblique to Z by 20–30°.

[31] We analyzed the quartz LPO of a foliation-parallel leucosome in a white mica-bearing migmatitic gneiss from the core of Mailolo Dome (sample 09-008a) separately from that of the adjoining residual host gneiss. The leucosome contains 22% quartz and preserves euhedral igneous feldspar grains (photomicrograph in Appendix B). The gneiss contains 38% quartz. Both yielded weak [c]-slip LPOs (J-values of 1.3 and 1.6, respectively). In other words, the LPO imprint of dislocation creep in quartz was similar in both samples despite their obvious differences in "final" melt proportion.

9. Other Fabric Changes With Increasing Structural Depth Into the Domes

9.1. Quartz LPO Strength

[32] As described above, the quartz LPOs that we measured in the foliated and lineated quartzofeldspathic gneisses yielded a set of recognizable patterns that were repeated in each dome. Especially in the highly "sheared" carapace-zone rocks, these LPOs were mostly weak (Table A and vertical bars on Figure 10). For most samples, the M index is in the range of 0.03 to 0.06, and the [c] axis J value is 1.2 to 2. The two measures of LPO strength are correlated, providing an identical relative ranking of LPO strengths across the sample set. A weak correlation exists between LPO strength and modal abundance of quartz, but only in those samples with >40–60% quartz (Figure 11a). The strongest LPOs occur in deformed quartz veins from the core zone (08, 011a, 08-037c, 08-071a, 10-048a, e.g., Figure 8m). These LPOs have J values of 4–11. The veins consist of 80–100% quartz, and have a typical unimodal maximum of [c] axes near X. Quartz-rich veins from the carapace zone, however, do not have such strong LPOs. For example, sample 10-021b from the carapace of Mailolo Dome consists of 99% quartz but has a [c]-axis J value of only 2.3. *Barth et al.* (2010) also observed very weak LPOs in HP to UHP gneisses from the Western Gneiss Region (WGR) of Norway. As in our study, *Barth et al.* found that LPO strength increased with increasing quartz

Figure 10. Plots showing variation in fabric parameters as a function of relative structural position in the D'Entrecasteaux Island domes. North is to the right; South is to the left. These include quartz LPO type, quartz fraction, LPO opening angle, and LPO fabric strength. Explanation of symbols is in lower left of figure.
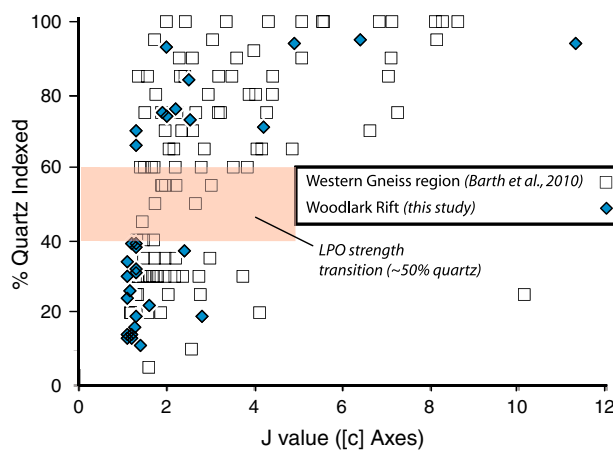
Figure 11. Scatter plot of Quartz LPO strength (J value of c-axes) vs modal percentage of quartz (% indexed).

fraction beyond a threshold modal quartz abundance of about 50% (see Figure 11a).

9.2. Quartz LPO Opening Angles

[33] The crossed-girdle opening angle of quartz c-axis LPOs may be a function of deformation temperature, hydrolytic weakening, or strain rate [*Tullis et al.*,

1973; *Lister & Hobbs*, 1980; *Kruhl*, 1998; *Law et al.*, 2004]. *Kruhl* [1998] suggested that the opening angles in plane strain may be used as a deformation thermometer, whereas *Law et al.* [2010] provided the caveat that the degree of dynamic recrystallization and non-plane strain deformation probably also affect the opening angle. Opening angles for our samples that featured [c]-axis crossed-girdles (and their
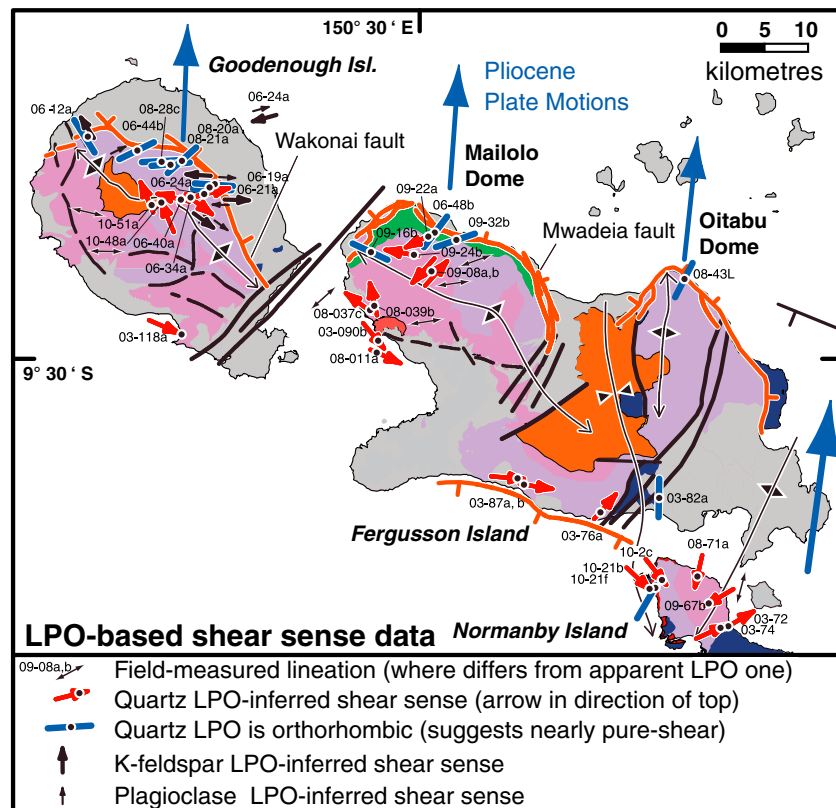

Figure 12. Shear-Sense Map. Map of NW D'Entrecasteaux Islands showing directions of ductile shearing (relative transport direction of top) as inferred from LPO data. Same geological patterns used as in Figure 2.

estimated uncertainty) are presented in Table B and Figure 10, and are also depicted on the complete set of [c]-axis pole figures (Appendix C). As expected, these angles broadly increase with increasing structural depth towards the dome cores. In the carapace zone, most opening angles are ~60–85°; whereas in the deeper core-zone rocks, they are either >90° or, most commonly, absent—because no crossed girdles exist in a [c]-slip LPO. Our interpretation of these in terms of increasing deformational temperature is reserved for the Discussion.

10. LPO-Determined Shear Senses in the Gneiss Domes

[34] Ductile shear-sense indicators in the carapaces of the D'Entrecasteaux gneiss domes were inferred from outcrop and microstructural observations by *Little et al.* [2011]. These shear senses were interpreted to represent the local syn-exhumational sense of shear that existed during the amphibolite-facies retrogression. While noting a dominance of top-E shear sense across the domes, *Little et al*. described a regional pattern of mixed top-E and top-W shear. In the carapace rocks, the shear-sense microstructures that they recognized included white-mica fish; oblique quartz GSFs; extensional (C') shear bands; asymmetric feldspar porphyroclasts; and other -objects, such as deformed boudins [*Little et al*., 2011]. In the carapace, extensional shear bands occur in conjugate sets (e.g., Figures 5f and 6c; see also Appendix B, samples 03-076a, 06-021a, and 06-048b), whereas in the core-zone rocks microstructural shear-sense indicators are typically absent, and only LPO data can be used to infer shear sense.

[35] Shear senses derived from our new quartz LPO data (red arrows in Figure 12) reinforce the pattern of bidirectional shear (and bulk coaxial deformation) throughout the D'Entrecasteaux Island domes. For example, two samples from the same outcrop of migmatitic gneiss in the core of Mailolo Dome (samples 09-008a, 09-008b) yield [c]-slip LPOs of opposite asymmetry, implying a reversal of shear sense on the scale of one meter. Moreover, most of the quartz LPOs that we measured in the carapaces are orthorhombic, implying nearly coaxial deformation at the thin-section scale in those samples (blue bars in Figure 12).

[36] In six samples of core-zone rocks from the SW sides of Goodenough and Mailolo domes, we had to rotate the LPOs about the foliation pole in order to obtain a typical [c]-slip or transitional to [c]-slip LPO (Figure 12). In every case, this rotation implied that the LPO-defined X direction was more NW–SE trending than the more nearly E–W lineation measured in the field (the latter are indicated with double arrows on Figure 12). Although other interpretations are possible, we follow *MacCready* [1996] in interpreting such discordance as providing a record of late-incremental maximum elongation that was discordant to the overall finite strain and thus the field-observed finite lineation. If so, this non-coaxial overprint was localized to the SW flanks of the two domes.

11. Chessboard Patterns and Oblique GSFs in Quartz

[37] A conspicuous feature of the core-zone gneisses is abundant deformation bands in quartz. These typically occur in two orthogonal sets (Figure 4a). Moreover, chessboard patterns are common (Figure 4c). In addition, some quartz grains in the core zone have nearly orthogonal (reticular) high-angle boundaries with other quartz grains (Figure 4a). As documented above, core-zone rocks typically display a quartz LPO that includes a maximum of [c] axes on the perimeter at ~30° to X. We have inferred shear sense in these rocks based on the asymmetry of this [c] axis maximum to the foliation. Quartzose rocks such as deformed veins typically contain strong GSFs in which the long axes of the quartz grains are oblique to the foliation. Several types of grain-shape obliquity were observed: (1) the long axes of the recrystallized quartz grains are inclined ~50–65° to the foliation plane (samples 08-37b, 08-39b, Figures 4a and 7c); or (2) they are inclined ~30° to the foliation plane (samples 09-67b, 10-48a, and 10-51a; or (3) both inclinations exist in different parts of one sample (Figure 13a). The ~50–65° GSFs are inclined with respect to the foliation in a sense that is synthetic with respect to the LPO-determined shear sense. At least in greenschist-facies mylonitic rocks, most oblique GSFs in domains of monomineralic quartz are forward-inclined at <45° to the foliation [*Lister and Snoke*, 1984; *Law et al*., 1984; *Dell'Angelo and Tullis*, 1989]. We note that *Stipp et al*. [2002a] also observed oblique GSFs in quartz in the high-temperature (GBM) part of the Tonale mylonites that are disposed at >45° to the foliation—similar to our case 1 (above). In our samples described as case 2, GSFs in quartz are inclined at a low angle (~30°) with respect to the foliation and in every case they imply the opposite ("wrong") shear sense than that inferred from the asymmetry of the LPO in the rock. Considered in
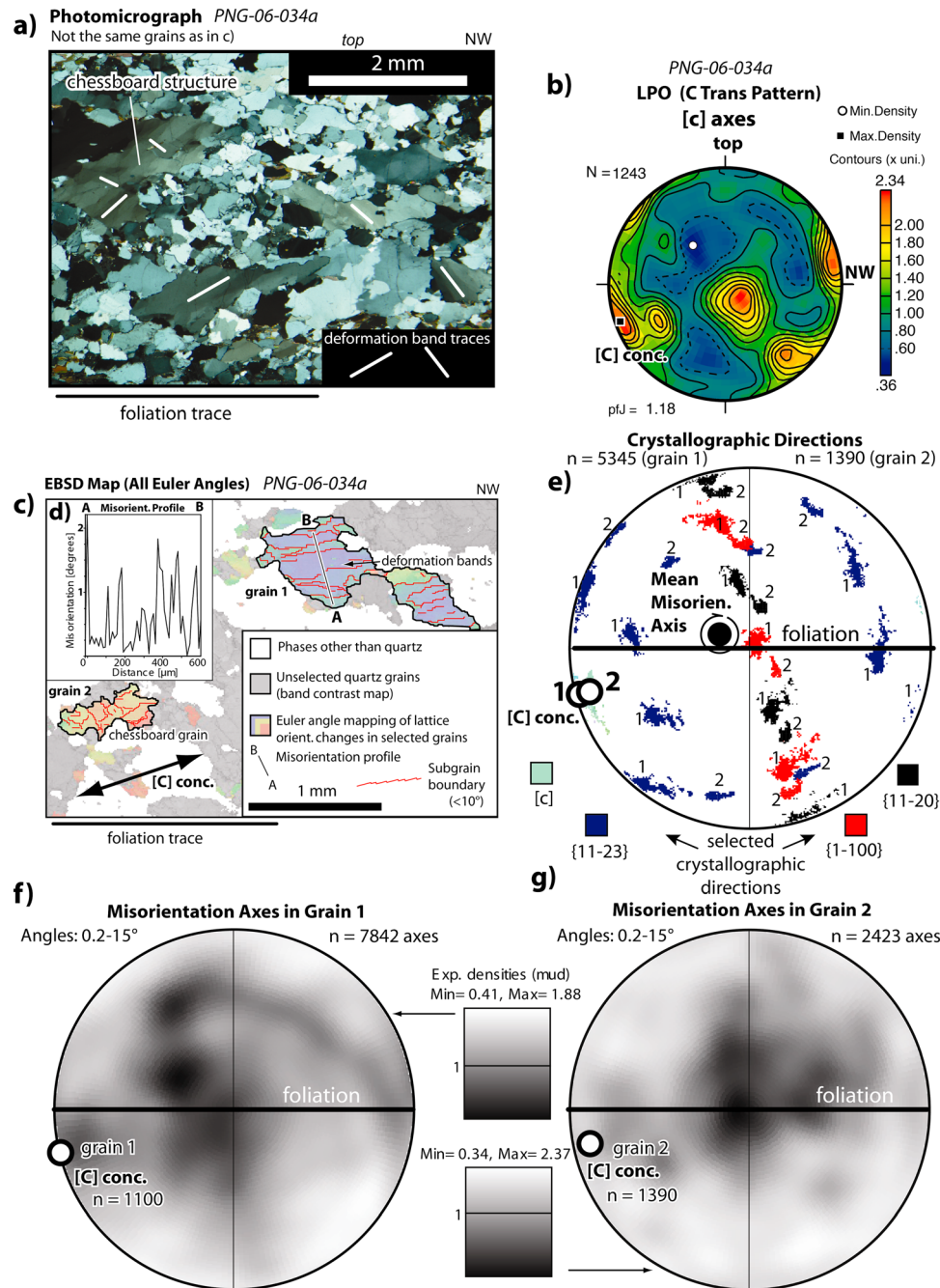
Figure 13. Crystallographic analysis of deformation banding and chessboard pattern of subgrains in quartz grains from core zone of Goodenough dome (sample 06-034a). All images are oriented with foliation horizontal, up on the top, and the NW lineation direction on the right. a) Optical photomicrograph (crossed Nicols) showing of deformation bands of chiefly NE-SW aspect (prismatic) and NW-SE aspect (basal) including some chessboard grains. Note the domainal nature of the quartz GSF, which tends to be parallel to one or the other of these directions. b) Pole figure of [c] axes from EBSD analysis. The dominant [c] axis maximum is labelled "[C] conc." c) EBSD derived Euler angle map showing outline two selected quartz grains that have [c] orientations subparallel to the maximum labelled in b. Grain 1 has prismatic deformation bands; grain 2 has a chessboard sub-grain pattern. d) Misorientation profile along the transect A-B across grain 1 showing deformation band related lattice rotations. e) Pole figure (in fabric reference frame) showing orientation of selected crystallographic directions for points inside grain 1 (labeled, "1") and in grain 2 (labeled, "2). The dispersion in these orientations indicates a rotation about a mean misorientation axis that is steeply plunging. f) Pole figure of low-angle (<15°) lattice misorientation axes that are internal to grain 1. Mean orientation of [c] axis for this grain is labelled. g) Pole figure of low-angle (<15°) lattice misorientation axes that are internal to grain 2. Mean orientation of [c] axis for this grain is labelled.

isolation, this predicts the wrong shear sense. We note that our observations on the relationship between on oblique quartz GSFs and deformation bands are remarkably similar to those made by *Law et al.* [1992] in quartz veins in high-temperature gneissic rocks near the Papoose Flat pluton in eastern California (see especially their Figures 5b and 7).

[38] Our EBSD data indicate that the oblique GSFs in recrystallized quartz aggregates are parallel to, and apparently controlled by, the orientation of deformation bands in that mineral, which, in turn are controlled by the LPO, which includes a unimodal concentration of [c] axes near X. Most of the deformation bands are either prismatic or basal, so the mixture of these two types yields a quasi-orthogonal pattern of deformation bands. The prismatic deformation bands are subparallel to the [c]-axis maximum, whereas the basal deformation bands are perpendicular to it (Figures 13a and 13b). Both orientations of deformation bands are commonly present in the same sample, but one may dominate a particular sample or portion of a sample. Where prismatic deformation bands dominate, a backward-inclined GSF at ~30° to the foliation is present (Figure 13b). Where basal deformation bands dominate, the deformation bands and any associated GSF tend to be inclined ~60° with respect to the foliation and inclined forward with respect to the shear direction. Rocks containing both orientations of deformation bands typically have a domainal GSF that varies spatially between these two configurations (e.g., samples 08-16b, 09-18a, 09-24b). The concordance between deformation band attitude and quartz GSF is not limited to rocks with the [c]-slip LPO. The same parallelism is also present in a deformed quartz vein that has a different, albeit still unimodal, [c]-axis LPO. This vein (sample 08-071a) has a strong [c] axis concentration at ~61° to the foliation, rather than at ~30°, perhaps recording an especially pronounced activity of basal-$<a>$ slip in this sample (Figure 7c). Our EBSD data for this sample reinforce the above-stated pattern: in this case, prismatic deformation bands in quartz grains are parallel to the [c] axis maximum, and also to the preferred direction of the long axes of recrystallized quartz grains in the sample (Figures 7c, 7d, and 7e).

[39] We determined that basal-$<a>$ and prism-[c] slip were both active in quartz at high temperature by misorientation analysis of sub-grain boundaries in grains that have a chessboard pattern of subgrains. In Figure 13c, quartz grains 1 and 2 both have their [c]-axes aligned approximately parallel to the [c] axis maximum in that rock (which is near X, see Figure 13b). Small (<2°) rotations of the crystal lattice across deformation band boundaries are

revealed in the misorientation profile, A-B (Figure 13d). The misorientation axes corresponding to these internal lattice distortions are plotted in a fabric reference frame for grain 1 in Figures 13e and 13f, and for grain 2 in Figure 13g. Note that most of these axes are perpendicular to [c]. Together with the observed alignment of the deformation bands both parallel and perpendicular to [c] (Figure 13a), this disposition of misorientation axes indicates combined slip on basal-$<a>$ and prism-[c] systems. A weak secondary maximum of misorientation axes parallel to [c] in grain 2 suggests additional prism-$<a>$ slip (Figure 13d).

12. Discussion

12.1. Evidence for Melt-Present Deformation

[40] The main phase of amphibolite-facies ductile deformation of the host gneisses took place in the presence of partial melt [*Hill*, 1994; *Little et al.*, 2011; *Gordon et al.*, 2012]. Criteria for identifying leucosomes (segregated melt) in these deformed migmatitic rocks include the occurrence of: (1) internally undeformed, coarse-grained, euhedral plagioclase grains that preserve growth zoning (often oscillatory); (2) melanocratic vein borders that are enriched in coarse-grained and euhedral (inferred peritectic) hornblende; and (3) vein margins that are diffuse or nebulitic. Where the most data exist, on Goodenough dome, centimetre-scale leucosome veins constitute 10–20% of typical carapace outcrops and up to 40% of outcrops in the deepest core rocks [these fractions were estimated using photographs of a 1×1 m grid placed over the outcrop, *Gordon et al.*, 2012]. The leucosomes are stromatic, vein-like or patch-like in morphology, and have been overprinted by variable degrees of solid-state deformation. Evidence for deformation in the presence of melt include: (1) grain-shape preferred orientation of euhedral feldspar and hornblende grains (interpreted as magmatic crystals) and/or the progressive rotational tiling of such grains towards parallelism with the foliation or the boundaries of melt-filled shears in the surrounding gneiss [Figure 4di]; and (2) accumulation of leucosome in deformation-induced dilation sites, such as boudin necks and strain shadows (Figures 4dii and 4diii). TIMS U-Pb dating of zircon in leucosomes and deformed granitoid dikes by *Gordon et al.* [2012] indicate that syntectonic leucosomes in Mailolo Dome crystallized at ~3.5–2.5 Ma.

[41] Although no other recognized UHP terranes contain as much former melt as the D'Entrecasteaux

Islands, others, including the WGR in Norway, do contain migmatites that formed at peak UHP conditions or after [e.g., *Labrousse et al.*, 2002, 2011; *Hacker et al.*, 2010]. In a global context, there is still much debate regarding the timing of partial melting of felsic rocks relative to their UHP burial [e.g., *Auzanneau et al.*, 2006; *Labrousse et al.*, 2011]; the role melting may play in the decoupling the UHP terranes from the downgoing plate [*Warren*, 2012]; and to what degree the ascent of UHP terranes to crustal depths and surface is driven by the added buoyancy provided by such melt [e.g., *Ellis et al.*, 2011]. The abundance of melt in the D'Entrecasteaux Islands is certainly consistent with the idea that it played a role in rheology and rapid exhumation of that terrane [e.g., *Lister & Baldwin*, 1993].

12.2. Interpretation of Quartz LPOs in the Gneiss Domes

[42] Quartz LPOs in the D'Entrecasteaux Islands affirm the activity of dislocation creep during exhumation of the UHP terrane from amphibolite-facies conditions. In addition, they provide a record of LPO changes as a function of structural depth (and presumably temperature) in rapidly exhumed gneiss domes. We interpret the mostly symmetric (orthorhombic) LPO fabrics in the carapace-zone rocks to record deformation that was largely coaxial and mostly approximately plane strain. Our data provides an important case study of LPO development in strongly deformed rocks that were undergoing GBM recrystallization, a fabric process that has not yet been analyzed using laboratory experiments.

[43] In the carapace zones, we interpret the small-circle LPOs to record slip on chiefly the basal-$<a>$ and rhomb-$<a>$ slip systems as a result of a coaxial strain that included flattening [e.g., *Lister and Hobbs*, 1980; *Schmid and Casey*, 1986]. By flattening, we refer to the general case where the Flinn strain shape parameter K is less than 1 and greater than 0. The Type-1 symmetric crossed-girdle patterns are taken to record a pure-shear dominated plane strain, for which the Flinn's parameter K is approximately 1.

[44] [e.g., *Lister*, 1977; *Law*, 1990]. The latter feature $<a>$ axes that are arranged in two maxima in the XZ plane disposed at similar acute angles to either side of X. The LPOs suggest a dominance of slip in the $<a>$ direction on the basal, rhomb, and prism planes. The cleft girdle LPOs are interpreted by us to have formed as a result of slip on the basal-$<a>$, rhomb-$<a>$, and possibly prism-$<a>$ slip systems during coaxial flow that was locally partly

constrictional, meaning that the Flinn's parameter is >1 and less than infinity [*Lister and Hobbs*, 1980; *Schmid and Casey*, 1986]. Experimental and numerical simulation studies indicate that type-2 crossed girdle fabrics form in plane to constrictional flows with symmetrical examples likely forming as a result of coaxial strain accumulation [*Jessel and Lister*, 1990; *Heilbronner and Tullis*, 2002; *Lister and Hobbs*, 1980; *Schmid and Casey*, 1986]. As one possible exception, sample 03-087b has $<a>$ axes distributed in a girdle through Y suggesting that the strain in this sample may have included some flattening (Figure 8h).

[45] In the core-zone rocks, we interpret the "transitional to [c]-slip" LPOs to have developed as prism-[c] slip became increasingly active relative to $<a>$ slip at upper amphibolite-facies temperatures. This LPO type (see also, *Stipp et al.*, 2002a; *Zibra et al.*, 2012) typically includes: (1) overlapping (co-linear) maxima of $<a>$ and [c] axes at a small angle to X; and (2) diffuse [c]-axis crossed girdles on the perimeter and/or through Y, similar to type-2 crossed girdles. For example, quartz vein (08-011a) includes a [c] axis maximum is in the XZ plane at a small angle to X that overlaps a $<a>$ axis maximum (Figure 8k). This co-linearity of [c] and $<a>$ axes suggests that slip took place parallel to both [c] and $<a>$. A second [c]-axis maximum is at a small angle to Z, where it overlaps with a concentration of {m}-poles. Such mutual concentrations of poles near Z are consistent with slip on both basal and prism planes. Another quartz-rich vein, 08-071a, yielded a strong maximum of [c] axes in the XZ plane at 20° to Z together with an $<a>$ axis maximum at ~20° to X (Figure 7c). This LPO may record dominance of basal-$<a>$ slip in this particular sample. *Keller & Stipp* [2011], citing a natural example deformed at $650 \pm 50\,°C$, alternatively proposed that such LPOs might form by a combination of {r}$<a>$, {z}$<a>$, and prism$<a>$ slip. In summary, the transitional-to-[c]-slip LPOs seem to reflect simultaneous activity of the basal-$<a>$, prism-[c], and prism-$<a>$ slip systems, a conclusion that is based on our analysis of slip systems based on the lattice misorientation axes associated with chessboard patterns of deformation bands in rocks with this LPO pattern (Figure 13).

[46] The [c]-slip LPOs are asymmetric featuring a single [c]-axis maximum in the XZ plane at a small angle to X. This suggests deformation that was both plane strain and non-coaxial [*Lister and Dornsiepen*, 1982; *Blumenfeld et al.*, 1986; *Okudaira et al.*, 1995; *Okudaira et al.*, 1998; *Kruhl*, 1998; *Fernandez et al.*, 2003]. On the basis of existing studies, we infer these to have formed as a result of predominantly prism-[c] slip at high temperature [>650°C,

Mainprice et al., 1986; *Okudaira et al.*, 1995; *Okudaira et al.*, 1998; *Kruhl*, 1998; *Barth et al.*, 2010; *Zibra et al.*, 2012]. Chessboard patterns in quartz in core-zone rocks suggest combined activity on prism-[c] slip and basal-$<a>$ slip at $>630\,°C$ [*Blumenfeld et al.*, 1986; *Mainprice et al.*, 1986; *Okudaira et al.*, 1995; *Takeshita* 1996; *Kruhl*, 1998; *Stipp et al.*, 2002a] argued, however, that water activity may decrease the minimum temperature to ~550°.

[47] The sense of shear in the core zone is mixed and bivergent. This supports the field-based inference of *Little et al.* [2011] that bulk deformation in the cores was approximately pure-shear deformation partitioned into conjugate shearing between lozenges of more competent rock bounded by shear zones that exploited local competence-contrast boundaries. Shear directions inferred from the asymmetry of LPOs of recrystallized grains (diameter $<200\,\mu$) of K-feldspar and plagioclase further reinforces the bivergent pattern of shear senses in the D'Entrecasteaux domes and are shown as black arrows on Figure 12, but the full LPO data for feldspar are not presented in this paper (see Table B in the auxiliary material). Non-plane deformation in the core zone is inferred for only three samples. Sample 10-048a combines the typical [c]-axis maximum near X with a girdle of $<m>$ poles (Appendix C) and may reflect a contribution of constrictional flow. Samples 03-090b and 09-067b have a distribution of [c] axes that is diffusely girdled between the fabric X axis and the fabric Y axis (Appendix C), and may reflect a somewhat oblate strain.

12.3. Comparison of Observed LPO Progression to That in Other Terranes

[48] The LPOs in this up-temperature fabric sequence appear to reflect a largely irrotational strain path that differs from that experienced by most crustal shear zones described in the literature. For example, the D'Entrecasteaux domes nowhere contain LPOs characterized by a strong [c]-axis concentration parallel to Y and/or a partial single girdle attached to Y, as is elsewhere quite typical of amphibolite-facies shear zones, and which has been interpreted to indicate a transition to primarily prism-$<a>$ slip in quartz [e.g., *Stipp et al.*, 2002a; *Toy et al.*, 2008; *Pennacchioni et al.*, 2010]. Unlike our gneisses, those in the core of the Saxony granulite terrane [*Lister and Dornsiepen*, 1982; their Figure 2] contain LPOs characterized by small-circle girdles of [c] axes disposed at ~40–50° to Z, which these authors suggest may reflect slip on pyramid

planes $\{2\bar{1}\bar{1}2\}$ in the direction $<c+a>$ and/or a competition between the basal $<a>$ and prism-[c] slip during an oblate strain. By contrast, the D'Entrecasteaux core-zone rocks consistently contain a single maximum of [c] in the XZ plane at 20–30° to X, an LPO that we attribute to dominant prism-[c] slip, a type of LPO that has also been seen in many other granulite and eclogite-facies terranes [e.g., *Blumenfeld et al.*, 1986; *Mainprice et al.*, 1986; *Okudaira et al.*, 1995; *Okudaira et al.*, 1998; *Kruhl*, 1998; *Fernandez et al.*, 2003; *Barth et al.*, 2010], and in felsic migmatitic rocks at near solidus temperatures [e.g., *Zibra et al.*, 2012].

[49] LPOs from the gneisses of the WGR differ from those in the D'Entrecasteaux domes in that the former are mostly single-girdles of [c] axes or maxima parallel to Y, with few type-I or type-II crossed-girdles (*Barth et al.*, 2010). This difference in LPOs may chiefly reflect a greater component of simple shear during exhumation of the WGR, particularly at high structural levels, a type of deformation mostly absent in the D'Entrecasteaux domes. On the other hand, both terranes share the following characteristics: (1) LPOs that record mainly amphibolite-facies plane strain to constriction, with fabrics consistent with being more common than those indicative of flattening; (2) the highest-grade rocks (including UHP eclogites in the WGR) have strong and asymmetric, single-crystal-like prism-[c] slip LPOs; (3) 10–100 km-wide domains in which the LPOs are mostly symmetric and/or variably asymmetric, recording coaxial deformation or bidirectional shear; and (4) relatively weak LPOs, increasing in strength slightly at quartz fractions $>50\%$.

12.4. Increase in Deformational Temperatures Inward into the Dome Cores

[50] Deformation temperatures increased inwardly toward the center of the domes—rather than outwardly or unidirectionally towards any bounding normal faults (or "detachments") on one side [*Burg et al.*, 2004; *Whitney et al.*, 2004; *Yin*, 2004].

[51] Increasing temperature with structural depth is apparently reflected by the transition in LPO types and from the crossed-girdle opening angle data as described above. Applying the calibration of *Kruhl* [1998] to our opening angles implies deformation temperatures of ~450 to ~650°C in the carapace rocks and ~700 to ~800°C in the core-zone rocks, although in detail the trend in opening angles is noisy (Figure 10). Because of the many uncertainties in the controlling parameters, these

temperatures cannot be considered to be precise. Part of the reason for this variability may be that the Kruhl [1998] thermometer is difficult to apply at deformation temperatures higher than ~650–700 °C because a wide range of opening angles are correlated to a small range of deformation temperatures. These temperature estimates are not unexpected given that temperatures of 700–800 °C have been previously inferred for the eclogite-facies metamorphism [Baldwin et al., 2004; Monteleone et al., 2007; Baldwin et al., 2008], that the felsic composition, migmatitic rocks underwent partial melting during their exhumation, and that peak temperatures of 625–700 ±30° have been estimated from Zr-in-Rutile thermometry for the syn-exhumational amphibolite-facies overprint [Korchinski et al., manuscript in review].

[52] Our inference that the core-zone LPOs record higher deformational (syn-exhumational) temperatures than the carapace-zone gneisses is supported by the Ti-in-Quartz thermometry of Korchinski et al. [2012] on the same sequence of gneisses. Thirty-five samples of carapace-zone rocks analyzed by LA-ICPMS yielded a mean apparent (minimum) temperature of ~540 ±20 °C using the Wark and Watson [2006] calibration. This is calibrated at 10 kb, which is approximately the pressure of the synkinematic (amphibolite facies) mineral assemblages. Forty-nine samples of core-zone rocks yielded a mean apparent (minimum) temperature of ~580 ±15 °C (1σ). Of these, 15 from the Goodenough dome yielded a mean apparent (minimum) temperature of 610 ±10°. Importantly, all four domes showed statistically robust trends of increasing temperature structurally downward [Korchinski et al., 2012]. These authors interpreted this thermometry, which consistently yields temperatures less than those implied by reaction isograds of synkinematic mineral assemblages, as providing a record of the average temperature of (final) GBM recrystallization (see also Grujic et al., 2011). We infer that the Ti-in-Quartz (apparent) temperatures were locked in during the final phases of the exhumation history, after the LPOs had already formed, when the gneiss domes were cooling very rapidly. The lower Ti-in-Quartz values may also reflect the lack of rutile in many of the analyzed samples.

[53] We note that the microstructure-based measures of deformational temperature, however imprecise, are higher for the core zone than are the corresponding Ti-in-Quartz recrystallization temperatures. A partially molten body that is rapidly exhumed is expected to undergo adiabatic decompression followed by rapid conductive cooling [e.g., Whitney

et al., 2004]. The existing thermobarometry supports such a thermal history for the D'Entrecasteaux domes—with $^{40}Ar/^{39}Ar$ data indicating cooling between ~400 and 120 °C at circa 100 °C/Myr after ~2 Ma [Baldwin et al., 1993; Baldwin et al., 2008]. Rapid cooling may thus have contributed to the inward temperature gradient that we have observed using microstructures. It also quenched-in unusually high-temperature microstructures for a crustally exhumed rock, including amoeboid quartz grains. Finally, we infer that the field gradient of inwardly increasing temperatures was enhanced as a result of the vertical collapse of the structural pile as a result of the pure-shear thinning that accompanied the exhumation of these rocks.

12.5. Kinematics of Ductile Flow and Exhumation of the Gneiss Domes through the Crust

[54] Only three of the eleven carapace samples yielded an asymmetric LPO. Moreover, two from the structurally outermost parts of that zone yielded small-circle [c]-axis LPOs, consistent with local 3D flattening strain [e.g., Lister and Hobbs, 1980; Schmid and Casey, 1986]. At greater depth, the samples indicate either plane strain (type-I crossed girdles, five samples) or constriction (cleft girdles, five samples). Farther down, near the base of the carapace, the seven samples yielding type-II crossed-girdle LPOs similarly suggest plane to constrictional flow. The data do not record unidirectional simple shearing, and thus do not support a detachment-driven core complex model for the D'Entrecasteaux terrane such as that proposed by Hill [1994] and Webb et al., [2008]. Instead, the LPO data support the idea that these are "pure-shear" gneiss domes in the sense of Yin [2004].

[55] The most dramatic phase of exhumation of the UHP terrane is from mantle depths (>90 km for coesite-bearing rocks) and took place at cm/year and approximately isothermally in the presence of partial melt but left little, if any, fabric record [Little et al., 2011]. Little et al. argued that the exhumation from mantle depths was driven by buoyancy of the partially molten, felsic UHP terrane with respect to the surrounding mantle, and by isostasy, as a result of rapid extension and thinning taking place in the Woodlark Rift to focus the ascent. Ellis et al. [2011] modelled the exhumation in 2D and 3D using the known plate motions in the boundary conditions, showing that such a diapiric model can explain the observed rates of exhumation, the dimensions of the exhumed UHP terrane, and key aspects of the

Woodlark rift structure, including the rift-margin-parallel (E–W) lineation trends. They showed that decompression melting would fuel the process (positive feedback) by increasing buoyancy and decreasing the viscosity of the rising UHP terrane. According to this model, the UHP terrane ascended into the upper plate of the former collision zone at a time when that upper plate was moving in an "absolute" sense away from the former subduction zone and towards the New Britain trench, a motion that drove the Woodlark Rift into extension. In some ways, the model resembles the geodynamic setting proposed for Eocene eclogite exhumation in the Western European Alps [*Malusa et al.*, 2011].

[56] We infer that the amphibolite-facies LPOs described in this paper formed after the UHP terrane first arrived in the lower crust and before it was finally emplaced upward as gneiss domes into the upper crust. By ~3 Ma, the partially exhumed UHP terrane had underplated the lower continental crust of the Woodlark Rift [*Gordon et al.*, 2012], perhaps to depths of >40 km, based on the inferred 11–14 kb pressure of the amphibolite-facies retrogression. During this retrogression, the UHP terrane acquired a regionally extensive, subhorizontal foliation as it thinned vertically and flowed horizontally [*Little et al.*, 2011]. Our LPO data record deformation that accompanied and/or post-dated development of this foliation, and they are consistent with largely coaxial deformation having accumulated in the currently exposed parts of the gneiss domes up until the time when the microstructures were frozen in. A key observation, moreover, is that the E–W direction of amphibolite-facies ductile extension in the domes is nearly orthogonal to the coeval Pliocene extension that took place in the overlying rift, implying that deformation of the rising gneiss body was decoupled from the Australia-Woodlark plate motion [Little et al., 2011]. Finally, by ~2 Ma [*Baldwin and Ireland*, 1995; *Ellis et al.*, 2011; *Gordon et al.*, 2012], the body had penetrated upward as several gneiss domes into the unmetamorphosed upper plate rocks of the Woodlark Rift, a final phase of deformation that warped the original foliation, and perhaps also constructively reinforced it. The gneiss domes then cooled rapidly. Finally, they were cut and tilted by normal faults, some of which remain active today.

12.6. Quartz Recrystallization and Grain-Growth Processes

[57] GBM recrystallization becomes an increasingly important recovery process at elevated temperature [e.g., *Urai et al.*, 1986; *Stipp et al.*, 2002b]. In the cores of the D'Entrecasteaux domes, amoeboid grain boundaries are common and straight grain boundary segments are rare. From this, we infer that significant static recrystallization did not affect these rocks. Instead, the rocks continued to deform until their microstructures were quenched as a result of the final phase of rapid, exhumation-related cooling. Most of the high-grade gneisses that we analyzed by EBSD in both the carapace and core zones have a (2-D) quartz grain size of 100–200 m. Based on observations of the rapidly cooled synkinematic aureole of the Adamello pluton in the European Alps, *Stipp et al.* [2002b] proposed that there are two different quartz recrystallization fields, GBM 1 and GBM 2, linked to the activity of GBM, separated by a temperature transition that lies somewhere between 560 ±30° and 650 ±30 °C. The higher temperature GBM 2 field is typified by deeply lobate quartz grains that developed without their boundaries being pinned by inclusions or other grain boundaries [case of non-impurity controlled grain boundary migration, *Stipp et al.* 2002a, 2002b]. The carapaces of the D'Entrecasteaux Islands domes include mica-pinned platy quartz "ribbon" grains, implying impurity-controlled GBM [GBM 1 field of *Stipp et al.*, 2002b]. By contrast, the core zones contain abundant amoeboid quartz grain boundaries with fewer obvious grain-pinning microstructures, similar to the GBM 2 field of *Stipp et al.* [2002b]. Such observations support the inward deformational temperature gradient that we discussed above.

[58] In this study, we report that deformation bands strongly influenced GBM in quartz in the core-zone gneisses. Grains tended to enlarge by their boundaries migrating along deformation bands in the consumed grain, rather than by sweeping across those sub-grain boundaries. Such behavior resembles that of experimentally deformed halite annealed at 350–400 °C [*Guillopé & Poirier*, 1979; *Piazolo et al.*, 2006]. Under such conditions, sub-grain boundaries in the deformed grains strongly control the mobility of grain boundaries as they migrate from new, relatively strain-free grains into older, more deformed grains [*Piazolo et al.*, 2006]. The migrating boundary tends to sweep selectively through one—but not the other—of two neighboring subgrains [*Piazolo et al.*, 2006]. At higher temperatures in halite (their regime III, >400 °C), grain boundaries tend to be less influenced by subgrains, to be longer and straighter, and to approach rational crystallographic planes of low interfacial free energy. Similar behavior has been suggested for quartz [*Kruhl and Peternell*, 2002]. The latter authors argued that this may explain the abundance [e.g., *Gapais and*

Barbarin, 1986] of planar, right-angle quartz grain boundary segments (reticular texture) in high-grade gneisses by the grain boundaries preferentially developing parallel to rhombohedral planes. Our LPO data in the D'Entrecasteaux rocks suggest that the above transition in GBM behavior takes place in quartz in the upper amphibolite facies at >550–650 °C.

[59] Anisotropy in rates of GBM with respect to deformation bands led to the development of oblique GSFs in quartz that mirrored the arrangement of the pre-existing deformation bands (e.g., Figures 4a and 4b). Dislocation creep in the veins produced LPOs with a strong [c]-axis maximum at a low angle to X. Because most of the deformation bands are either basal or prismatic (or both, in the case of chessboard patterned grains), the deformation bands are arranged in a quasi-orthogonal pattern relative to the [c]-axis maximum. Our EBSD mapping leads us to infer oblique GSFs in quartz may develop in high-grade gneisses primarily as a result of high-temperature GBM with rates of grain-boundary mobility controlled by sub-grain structure [see also, *Platt and Behr*, 2011]. In this case, oblique GSFs do not develop as a result of strain-related elongation of dynamically recrystallized quartz grains [*sensu Means*, 1981], and shear sense cannot be easily inferred from the observed obliquity. The sense of external obliquity of these fabrics to the foliation may be antithetic to the shear sense. We conclude that oblique GSFs in quartz should be avoided as a shear-sense indicator in high-grade gneisses.

12.7. Deformation Mechanisms in the UHP Terrane

[60] Our data affirm that dislocation creep was an important deformation mechanism during exhumation of the partially molten UHP terrane through the crust. The D'Entrecasteaux Island gneisses are high strain rocks, and they have undergone more than one transposition cycle [*Little et al.*, 2011]. Given this, other aspects of our data suggest that other mechanisms were also important. One line of evidence is that although the carapace gneisses—especially—are strongly foliated and lineated, their quartz LPOs are mostly weak, even where those rocks are quartz rich. Throughout the domes, the LPOs typically have [c]-axis J values of <2. A few of the deformed veins, consisting of >95% quartz, have stronger LPOs (Figure 11a). We concede that it is currently not possible to use such LPO strengths in deformed quartzofeldspathic rocks as a quantitative proxy for, or measure of, the relative contribution of dislocation creep. For a given quartz

content, we note that the D'Entrecasteaux gneisses have LPO strengths that are on average slightly less than (or similar to) those measured by EBSD in samples of amphibolite facies, quartzofeldspathic gneiss from the WGR in Norway [Figure 11a, *Barth et al.*, 2010]. We observe a weak positive correlation in both terranes between quartz abundance and quartz LPO intensity at quartz modal fractions >50%. If real, we infer that this transition probably does not reflect the development of an interconnected weak phase in the polyphase rocks; for example, at higher quartz contents, because such a rheological transition should occur at weak phase fractions of only 20–30% rather than >50% [e.g., *Handy*, 1994; *Holyoke and Tullis*, 2006]. Many have proposed that LPO weakness in deformed polyphase rocks implies activity of deformation mechanisms other than dislocation creep; for example *Stöckhert* [2002] with respect to high pressure rocks in the European Alps and in Crete; and *Barth et al.* [2010] with regard to the rocks in WGR of Norway. *Stöckhert* [2002] argued for dissolution-precipitation creep or fluid-assisted grain-boundary sliding at low differential stress in the Alpine rocks. Although speculative, we suggest that one obvious mechanism for reducing the importance of dislocation creep in the D'Entrecasteaux Islands migmatitic gneisses was the widespread presence of melt when rocks were being deformed (see above). Where melt was present at greater than the critical melt fraction (~7%), viscous melt flow could have taken place within the largely interconnected melt domains and along grain boundaries, causing a type of melt-assisted granular flow [e.g., *Dell'Angelo and Tullis*, 1988; *Rosenberg and Handy*, 2005]. Experimental data suggest that such a process could reduce the effective viscosity of the rock by >4 orders of magnitude relative to its subsolidus state [e.g., *Rosenberg and Handy*, 2005].

[61] Microstructures in plagioclase and K-feldspar also affirm the activity of dislocation creep in those minerals. For example, some porphyroclasts have undulatory extinction, and/or sub-grain structures (e.g., Figure 5d) [e.g., *Tullis*, 2002]. Deformation of plagioclase and K-feldspar by SGR-accommodated dislocation creep is consistent with core-zone deformation temperatures of >600–650 °C [*Vidal et al.*, 1980; *Olsen and Kohlstedt*, 1985; *Pryer*, 1993; *Altenberger and Wilhelm*, 2000; *Kruse et al.*, 2001; *Tullis*, 2002; *Rosenberg and Stunitz*, 2003]. This accords with our quartz microstructural observations, with the observation that deformation took place during partial melting of the rocks, and with existing petrologic constraints on temperature during the amphibolite-facies retrogression (570–730 °C, *Hill*,

and Baldwin, 1993). And yet most feldspar porphyroclasts appear almost undeformed, with delicate primary internal structures such as oscillatory growth zoning, lamellar or simple growth twins, and exsolution lamellae (e.g., Figures 5a and 5c), and they are surrounded by a finer-grained, polyphase matrix of dispersed feldspar + quartz + mica (e.g., Figure 5b). Using EBSD we measured the crystallographic orientation of the $<250\,\mu$ fraction of plagioclase or K-feldspar grains (or both) in 13 of the 37 samples, finding weak feldspar LPOs in nine of these 13 and nearly random or irregularly domainal LPOs in the other four. The LPOs most commonly suggest activity of the (010) [100] or (010) [001] slip systems (see Table B). The LPOs are weak, with most of the feldspar LPOs having M values of 0.03–0.06 (maximum of ~0.10). As is the case with quartz, the weakness of these LPOs in such strongly foliated and lineated rocks is at least consistent with dislocation creep not being the only deformation mechanism. Moreover, plagioclase and K-feldspar grains are truncated along planes parallel to the foliation, most commonly against deeply impinging quartz grains (Figures 5c and 5e). The lobate–cuspate microstructure suggests that the feldspar-dissolving reactions were incongruent, with quartz being a product phase. Strain shadows and veins at a high angle to the stretching lineation record the syndeformational reprecipitation of K-feldspar, plagioclase, biotite and quartz (e.g., Figures 5e and 7b). Similar precipitation of new K-feldspar grains in dilatational sites has been described in high-grade gneisses by *Wintsch and Yi* [2002] and *Ishii et al.* [2007] and in lower amphibolite-facies rocks by *Kilian et al.* [2011]. From these microstructural observations we infer that feldspar underwent deformation by fluid-assisted grain-boundary diffusion creep together with some dissolution and reprecipitation [see also, *Gower and Simpson*, 1992; *Martelat et al.*, 1999; *Wintsch and Yi*, 2002; *Rybacki and Dresen*, 2004; *Kilian et al.*, 2011]. It is possible that melt may have enhanced rates of diffusion creep in these migmatitic rocks [e.g., *Dell'Angelo and Tullis*, 1988; *Zavada et al.*, 2007]. Finally, we note that, in addition, localized slip took place in mica films that wrap coarser, lens-shaped feldspar grains, presumably by dislocation glide within the weak phyllosilicate film (Figure 5b; Figures 6c and 6d). This suggests deformation may have been accommodated by a weak-phase controlled type of grain-boundary-sliding [see also, for example, *Rosenberg and Stunitz*, 2003; *Holyoke and Tullis*, 2006].

13. Conclusions

[62] The world's youngest UHP terrane is internally strongly deformed. After recrystallizing at UHP conditions, the rocks are inferred to have risen buoyantly through the mantle wedge overlying the Papuan paleo-subduction zone as partially molten diapirs [*Little et al.*, 2011] at rates of >1 cm/yr [*Baldwin et al.*, 2008]. At ~3 Ma [*Gordon et al.*, 2012], the gneisses underplated the lower crust of the Woodlark Rift, where they underwent amphibolite-facies retrogression. There, the UHP terrane began to spread laterally subparallel to the margins of Woodlark Rift [*Little et al.*, 2011]. By ~2 Ma [*Baldwin & Ireland*, 1995; *Gordon et al.*, 2012], the partially molten body was emplaced into the upper crust as gneiss domes. This diapiric emplacement precipitated rapid cooling of the domes at >100 °C/Myr [*Baldwin et al.*, 1993], a process that quenched-in and preserved young, high-temperature microstructures.

[63] Microstructures and quartz LPOs in the UHP-bearing gneissic terrane of the D'Entrecasteaux Islands provide insight into: (1) the kinematics of flow affecting these migmatitic gneisses in the lower crust of the Woodlark Rift; and (2) the high-temperature deformation processes that affected them prior to their rapid ascent into the upper crust, at which time their microstructures were quenched-in as a result of rapid cooling.

[64] The quartz LPOs in the D'Entrecasteaux Islands UHP terrane affirm the activity of dislocation creep during the exhumation of the terrane from lower crustal depths. Each of the gneiss domes yielded a similar progression of LPOs. With increasing structural depth, the sequence of [c]-axis LPOs in these domes is: (1) small circle LPOs; followed by either type-1 crossed-girdles or cleft-girdles; followed by (2) type-2 crossed-girdles; followed by (3) a transitional LPO resulting from combined basal -<a> and prism-[c] slip; followed by (4) a prism-[c] slip LPO, typically with a nearly "single-crystal" type of LPO throughout the cores of the gneiss domes. This sequence of LPOs (including the opening angles of crossed-girdle fabrics and the transition from <a> slip to [c] slip in quartz) suggest that deformation temperatures increased towards the dome centers, a trend that is mirrored by variations in Ti-in-Quartz apparent (minimum) temperature [*Korchinski et al.*, 2012]. Microstructures and LPOs imply deformational temperatures of perhaps 450 to 650 °C in the carapaces of these domes and >650 °C in the core zones. There, amoeboid grain-boundaries

and chessboard patterns of subgrains are common in quartz, and the modal fraction of leucosome in the migmatites is 15–70% [*Gordon et al.*, 2012].

[65] The LPOs in gneisses of the outer carapace zones are mostly orthorhombic, recording a dominantly irrotational and plane (pure-shear) deformation during exhumation of these rocks through the crust. This flow thinned the rocks vertically, probably exaggerating the field gradient of inwardly increasing deformational temperatures that was a result of conductive cooling of the rapidly exhumed, migmatitic domes. In the deeper cores of the domes, non-coaxial deformation prevailed at the microstructural and mesoscopic scale; however, the regional pattern of shearing throughout the gneiss domes is bidirectional, reflecting a conjugate shearing between lozenges of variably competent rocks in a bulk deformation regime that remained approximately coaxial [*Little et al.*, 2011]. Others [e.g., *Hill*, 1994; *Baldwin et al.*, 2004] have referred to the carapace zones as being mylonitic "shear zones". If so, it is our view that these zones have undergone largely a "pure" shearing. Moreover, we [also *Hill*, 1994] note that the grain size of the carapace rocks is not obviously reduced relative to that of the adjacent core, which suggests that flow stresses were not markedly higher in the "sheared" outer carapaces rocks.

[66] In core-zone rocks, deformation bands in quartz influenced the shape of quartz-quartz grain boundaries formed during high-temperature GBM recrystallization. The long dimensions of recrystallized quartz grains preferentially developed parallel to precursory quasi-orthogonal sets of basal and prismatic deformation bands. The resulting (commonly bidirectional) oblique GSFs seem to have been controlled by sub-grain controlled anisotropic grain growth rather than by progressive shear deformation of originally more equant, dynamically recrystallized grains [as originally suggested by *Means* 1981]. From this relationship, we conclude that oblique GSFs are a problematic shear-sense indicator in high-grade gneisses.

[67] Dislocation creep was an important deformation mechanism during exhumation of the quartzofeldspathic gneisses. Other likely mechanisms include: (1) melt-assisted granular flow in migmatites with >7% intergranular melt; (2) fluid-assisted grain-boundary diffusion creep in conjunction with localized dissolution and reprecipitation of K-feldspar; and (3) localized dislocation glide in mica films that wrap feldspar grains.

References

Abers, G. A., A. Ferris, M. Craig, H. Davies, A. Lerner-Lam, J. C. Mutter, and B. Taylor (2002), Mantle compensation of active metamorphic core complexes at Woodlark rift in Papua New Guinea, *Nature*, *418*, 862–865.

Altenberger, U., and S. Wilhelm (2000), Ductile deformation of K-feldspar in dry eclogite facies shear zones in the Bergen Arcs, Norway, *Tectonophysics*, *320*, 107–121.

Auzanneau, E., D. Vielzeuf, and M. W. Schmidt (2006), Experimental evidence of decompression melting during exhumation of subducted continental crust, *Contrib. Mineral. Petrol.*, *152*, 125–148.

Baldwin, S. L., and T. R. Ireland (1995), A tale of two eras: Plio-Pliestocene unroofing of Cenozoic and late Archean zircons from active metamorphic core complexes, Solomon Sea, Papua New Guinea, *Geology*, *23*, 1023–1026.

Baldwin, S. L., G. S. Lister, E. J. Hill, D. A. Foster, and I. McDougall (1993), Thermochronologic constraints on the tectonic evolution of active metamorphic core complexes, D'Entrecasteaux Islands, Papua New Guinea, *Tectonics*, *12*, 611–628.

Baldwin, S. L., P. G. Fitzgerald, and L. E. Webb (2012), Tectonics of the New Guinea Region, *Ann. Rev. Earth Planetary Sci.*, *40*, 495–520.

Baldwin, S. L., B. Monteleone, L. E. Webb, P. G. Fitzgerald, M. Grove, and J. Hill (2004), Pliocene eclogite exhumation at plate tectonic rates in eastern Papua New Guinea, *Nature*, 8, doi:10.1038/nature02846.

Baldwin, S. L., L. E. Webb, and B. D. Monteleone (2008), Late Miocene coesite-eclogite exhumed in the Woodlark Rift, *Geology*, *36*, 735–738.

Barth, N. C., B. R. Hacker, G. E. Seward, E. O. Walsh, D. Young, and S. Johnston (2010), Strain within the Ultrahigh-Pressure Western Gneiss Region of Norway recorded by Quartz CPOs, *Geol. Soc. Spec. London Publ.*, *335*, 663–685, doi:10.1144/SP335.27.

Blumenfeld, P., D. Mainprice, and J.-L. Bouchez (1986), c-Slip in quartz from subsolidus deformed granite, *Tectonophysics*, *127*, 97–115.

Bunge, H.-J. (1977), *Texture Analysis in Materials Science*, pp. 593, Butterworth's, London.

Burg, J.-P., B. J. P. Kaus, and Y. Y. Podlachikov (2004), Dome structures in collision orogens: Mechanical investigation of the gravity/compression interplay, in *Gneiss Domes in Orogeny*, edited by D. L. Whitney, C. Teyssier, and C. S. Siddoway, pp. 47–66, Geological Society of America, Boulder, CO.

Daczko, N., P. Caffi, J. L. Halpin, and P. Mann (2009), Exhumation of the Dayman dome metamorphic core complex, eastern Papua New Guinea, *J. Metamorph. Geol.*, *27*, 405–422.

Davies, H., and R. G. Warren (1988), Origin of eclogite-bearing, domed, layered metamorphic complexes ("core complexes") in the D'Entrecasteaux islands, Papua New Guinea, *Tectonics*, 7, 1–21.

Davies, H. L. (1973), The Geology of Fergusson Island, *map with explanatory notes*, Australia Bureau of Mineral Resources.

Davies, H. L. (1980), Folded thrust fault and associated metamorphics in the Suckling-Daymon massif, Papua New Guinea, *Am. J. Sci.*, *280A*, 171–191.

Davies, H. L. (2012), The geology of New Guinea - the cordilleran margin of the Australian continent, *Episodes*, 35, 87–102.

Davies, H. L., and A. L. Jaques (1984), Emplacement of ophiolite in Papua New Guinea, *Geol. Soc. Spec. London Publ.*, *13*, 341–350.

Dell'Angelo, L. N., and J. Tullis (1988), Experimental deformation of partially melted granitic aggregates, *J. Metamorph. Geol.*, *6*, 495–515.

Dell'Angelo, L. N., and J. Tullis (1989), Fabric development in experimentally sheared quartzites, *Tectonophysics*, *169*, 1–21.

Ellis, S., T. A. Little, L. Wallace, B. Hacker, S. M. Gordon, and S. Buiter (2011), Feedback between rifting and diapirism drives UHP exhumation in the Woodlark Basin, *Earth Planet. Sci. Lett.*, *311*(3–4), 427–483.

Ernst, W. G. (2001), Subduction, ultrahigh-pressure metamorphism, and regurgitation of buoyant crustal slices-implications for arcs and continental growth, in *Processes and Consequences of Deep Subduction*, Physics of Earth and Planetary Inte-riors, Vol. 127, Issue 1-4, edited by D. Rubie and R. van der Hilst, pp. 253–275, Elsevier Science B.V.

Fernandez, F. J., H. I. Chamine, P. E. Fonseca, J. M. Manha, A. Ribeiro, J. Aller, M. Fuertes-Fuentes, and F. S. Borges (2003), HT-fabrics in a garnet-bearing quartzite from western Portugal: geodynamic implications for the Iberian Variscan Belt, *Terra Nova*, *15*(2), 96–103.

Francis, G., G. Lock, and Y. Okuda (1987), Seismic straigraphy and structure of the area to the southeast of the Trobriand Platform, *Geo-Mar Lett.*, *7*, 121–128.

Gapais, D., and B. Barbarin (1986), Quartz fabric transition in a cooling syntectonic granite (Hermitage massif, France), *Tectonophysics*, *125*, 357–370.

Goodliffe, A., B. Taylor, F. Martinez, R. Hey, K. Maeda, and K. Ohno (1997), Synchronous reorientation of the Woodlark basin spreading center, *Earth Planet. Sci. Lett.*, *146*, 233–242.

Gordon, S. M., T. A. Little, B. R. Hacker, S. A. Bowring, M. Korchinski, S. L. Baldwin, A. R. C. Kylander-Clark, and M.-A. Millet (2012), Multi-stage exhumation of young UHP–HP rocks: timescales of melt crystallization in the D'Entrecasteaux Islands, southeastern Papua New Guinea, *Earth Planet. Sci. Lett.*, *351–352*, 237–246.

Gower, R. J. W., and C. Simpson (1992), Phase boundary mobility in naturally deformed deformed, high-grade quartzofeldspathic rocks: Evidence fopr diffusion creep, *J. Struct. Geol.*, *14*, 301–314.

Guillopé, M., and J. P. Poirier (1979), Dynamic recrystallization during creep of single-crystalline halite: an experimental study, *J. Geophys. Res.*, *84*, 5557–5567.

Grujic, D., M. Stipp, and J. Wooden (2011), Thermometry of quartz mylonites: Importance of dynamic recrystallization on Ti-in-quartz re-equilibration, *Geochem. Geophys. Geosyst.*, *12*, Q06012, doi:10.1029/2010GC003368.

Hacker, B. (1996), Eclogite formation and the rheology, buoyancy, seisimicity, and H_2O content of oceanic crust, in *Subduction Top to Bottom*, edited by G. E. Bebout, D. W. Scholl, S. H. Kirby, and J. P. Platt, pp. 337–346, American Geophysical Union, Washington, D. C.

Hacker, B. R., T. B. Andersen, A. R. C. Kylander-Clark, S. M. Johnstone, E. Peterman, E. O. Walsh, and D. Young (2010), High-tempreture deformation during continental-margin subduction and exhumation: The ultrahigh-pressure western Gneiss Region of Norway, *Tectonophysics*, *480*, 149–171.

Hall, R. (2002), Cenozoic geological and plate tectonic evolution of SE Asia and the SW Pacific: computer-based reconstructions, model and animations, *J. Asian Earth Sci.*, *20*, 353–431.

Handy, M. R. (1994), Flow laws for rocks containing two non-linear viscous phases: a phenomological approach, *J. Struct. Geol.*, *16*, 287–301.

Heilbronner, R., and J. Tullis (2002), The effect of strain annealing on microstructure and crystallographic preferred orientations of quartzites experimentally deformed in axial compresion and shear, in *Deformation Mechanisms, Rheology, and Tectonics: Current Status and Future Perspectives*, edited by S. De Meer, et al., pp. 191–218, Geological Society of London, London.

Heilbronner, R., and J. Tullis (2006), Evolution of c axis pole figures and grain size during dynamic recrystallization: Results from experimentally sheared quartzite, *J. Geophys. Res.*, *111*, B10202.

Hill, E. J. (1994), Geometry and kinematics of shear zones formed during continental extension in eastern Papua New Guinea, *J. Struct. Geol.*, *16*, 1093–1105.

Hill, E. J., and S. L. Baldwin (1993), Exhumation of high-pressure metamorphic rocks during crustal extension in the D'Entrecasteaux region, Papua New Guinea, *J. Metamorph. Geol.*, *11*, 261–277.

Hill, E. J., S. L. Baldwin, and G. S. Lister (1992), Unroofing of active metamorphic core complexes in the D'Entrecasteaux Islands, Papua New Guinea, *Geology*, *20*, 907–910.

Holcombe, R. J. (2008), Georient (v.9) [computer program], http://www.holcombe.net.au/software/rodh_software_georient.htm.

Holyoke, C. W., III, and J. Tullis (2006), Mechanisms of weak phase interconnection and the effects of phase strength contrast on fabric development, *J. Struct. Geol.*, *28*, 621–640.

Ishii, K., K. Kanagawa, N. Shigematsu, and T. Okudaira (2007), High ductility of K-feldspar and development of granitic banded ultramylonite in the Ryoke metamorphic belt, SW Japan, *J. Struct. Geol.*, *29*(6), 1083–1098.

Jessel, M. W., and G. S. Lister (1990), A simulation of the temperature dependence of quartz fabrics, in *Deformation Mechanisms, Rheology, and Tectonics*, edited by R. J. Knipe, and E. H. Rutter, pp. 353–362.

Keller, L. M., and M. Stipp (2011), The single-slip hypothesis revisited: Crystal-preferred orientations of sheared quartz aggregates with increasing strain in nature and numerical simulation, *J. Struct. Geol.*, *33*, 1491–1500.

Kilian, R., R. Heilbronner, and H. Stünitz (2011), Quartz grain size reduction in a granitoid rock and the transition from dislocation to diffusion creep, *J. Struct. Geol.*, *33*, 1265–1284.

Korchinski, M. (2011), Ascent of ultrahigh-pressure in southeastern Papua New Guinea, as revealed by Ti-in-quartz thermometry and Rb/Sr dating, M. Sc. thesis, 162 pp., Victoria Universty of Wellington, Wellington, New Zealand.

Korchinski, M., T. A. Little, E. G. C. Smith, and M. A. Millet (2012), Variation of Ti-in-quartz in gneiss domes exposing the world's youngest ultrahigh-pressure rocks, D'Entrecasteaux Islas, Papua New Guinea, *Geochem. Geophys. Geosyst.*, doi:10.1029/2012GC004230.

Korchinski, M., et al. (in review), Timing of UHP exhumation and rock fabric development in gneiss domes containing the world's youngest eclogite-facies rocks,

Woodlark Rift, southeastern Papua New Guinea, *J. Metamorph. Geol.*

Kruhl, J. H. (1998), Prism- and basal-plane parallel subgrain boundaries in quartz: a microstructural geothermobarometer, *J. Metamorph. Petrol.*, *16*, 142–146.

Kruhl, J. H., and M. Peternell (2002), The equilibration of high-angle grain boundaries in dynamically recrystallized quartz: the effect of crystallography and temperature, *J. Struct. Geol.*, *24*, 1125–1137.

Kruse, R., H. Stunitz, and K. Kunze (2001), Dynamic recrystallization processes in plagioclase porphyroclasts, *J. Struct. Geol.*, *23*, 1781–1802.

Labrousse, L., L. Jolivet, R. Agard, R. Hebert, and T. B. Andersen (2002), Crustal-scale boudinage and migmitization of gneiss during their exhumation in the UHP Province of western Norway, *Terra Nova*, *14*, 263–270.

Labrousse, L., G. Prouteau, and A. C. Ganzhorn (2011), Continental exhumation triggered by partial melting at ultrahigh pressure, *Geology*, *39*, 1171–1174.

Law, R. D. (1990), Crystallographic fabrics: a selective review of their applications to research in structural geology, in *Deformation Mechanisms, Rheology and Tectonics*, edited by R. J. Knipe and E. H. Rutter, pp. 335–352, Geological Society of London Special Publication 54, London U.K.

Law, R. D., R. J. Knipe, and H. Dayan (1984), Strain path partitioning within thrust sheets: microstructural and petrofabric evidence from the Moine Thrust zone at loch Eriboll, northwest Scotland, *J. Struct. Geol.*, *6*, 477–497.

Law, R. D., S. M. Morgan, M. Casey, A. G. Sylvester, and M. Nyman (1992), The Papoose Flat pluton of eastern California: a reassessment of its emplacement history in the light of new microstructural and crystallographic fabric observations, *Trans. R. Soc. Edinburgh: Earth Sci.*, *83*, 361–375.

Law, R. D., M. P. Searle, and R. L. Simpson (2004), Strain, deformation temperatures and vorticity of flow at the top of the Greater Himalayan Slab, Everest Massif, Tibet, *J. Geol. Soc. London*, *161*, 305–320.

Law, R. D., D. H. Mainprice, M. Casey, G. E. Lloyd, R. J. Knipe, B. Cook, and J. R. Thigpen (2010), Moine thrust zone mylonites at the stack of Glencoul1–microstructures, strain and influence of recrystallization of quartz crystal fabric development, in *Continental Tectonics and Mountain Building– The Legacy of Peach and Horne*, edited by R. D. Law, R. W. H. Butler, R. E. Holdsworth, M. Krabbendam, and R. Strachen, pp. 543–577, Geological Society of London, Special Publications 335, London U.K.

Lenze, A., and B. Stöckhert (2007), Microfabrics of UHP metamorphic granites n the Dora Maira Massif, western Alps- no evidence of deformation at great depth, *J. Metamorph. Geol.*, *25*, 461–474.

Lister, G. S. (1977), Discussion: crossed-girdle c-axis fabrics in quartzites plastically deformed gy plane starin and progressive simple shear, *Tectonophysics*, *39*, 51–54.

Lister, G. S., and B. E. Hobbs (1980), The simulation of fabric development during plastic deformation and its application to quartzite: the influence of deformation history, *J. Struct. Geol.*, *2*, 355–370.

Lister, G. S., and U. F. Dornsiepen (1982), Fabric transitions in the Saxony granulite terrain, *J. Struct. Geol.*, *4*, 81–92.

Lister, G. S., and S. L. Baldwin (1993), Plutonism and the origin of metamorphic core complexes, *Geology*, *21*, 607–610.

Lister, G. S., and A. W. Snoke (1984), S-C mylonites, *J. Struct. Geol.*, *6*, 617–638.

Little, T. A., S. L. Baldwin, P. G. Fitzgerald, and B. Monteleone (2007), Continental rifting and metamorphic

core complex formation ahead of the Woodlark Spreading Ridge, D'Entrecasteaux Islands, Papua New Guinea, *Tectonics*, *26*, TC1002, doi:10.1029/2005TC001911.

Little, T. A., B. R. Hacker, S. M. Gordon, S. L. Baldwin, P. G. Fitzgerald, S. Ellis, and M. Korchinski (2011), Diapiric exhumation of the world's youngest (UHP) eclogites in the gneiss domes of the D'Entrecasteaux Islands Papua New Guinea, *Tectonophysics*, *30*, doi:10.1016/j.tecto.2011.06.006.

Lus, W. Y., I. McDougall, and H. L. Davies (2004), Age of the metamorphic sole of the Papuan Ultramafic Belt ophiolite, Papua New Guinea, *Tectonophysics*, *392*, 85–101.

MacCready, T. (1996), Misalignment of quartz c-axis fabrics and lineations due to oblique final strain increments in the Ruby Mountains core complex, Nevada, *J. Struct. Geol.*, *18*, 765–776.

Mainprice, D. (2005), PFch5 [Computer Software], ftp://www.gm.univ-montp2.fr/mainprice//CareWareUnicef Programs/.

Mainprice, D., J.-L. Bouchez, P. Blumenfeld, and J. M. Tubia (1986), Dominant c slip in naturally deformed quartz: Implications for dramatic plastic softening at high temperature, *Geology*, *14*, 819–822.

Malusa, M. G., C. Faccenna, E. Garzanti, and R. Polino (2011), Divergence in subduction zones and exhumation of high pressure rocks (Eocene Western Alps), *Earth Planet. Sci. Lett.*, *310*, 21–32.

Martelat, J. E., K. Schulmann, J. M. Lardeaux, C. Nicollet, and H. Cardon (1999), Granulite microfabrics and deformation mechanisms in southern Madagascar, *J. Struct. Geol.*, *21*, 671–687.

Martinez, F., A. Goodliffe, and B. Taylor (2001), Metamorphic core complex formation by density inversion and lower crustal extrusion, *Nature*, *411*, 930–933.

Means, W. D. (1981), The concept of the steady-state foliation, *Tectonophysics*, *78*, 179–199.

Monteleone, B. D., S. L. Baldwin, L. E. Webb, P. G. Fitzgerald, M. Grove, and A. K. Schmitt (2007), Late Miocene-Pliocene eclogite-facies metamorphism, D'Entrecasteaux Islands, SE Papua New Guinea, *J. Metamorph. Geol.*, *25*(Special Volume on Ultrahigh Pressure Metamorphism in honor of J. G. Liou), 245–265.

Mulchrone, K. F., F. O'Sullivan, and P. A. Meere (2003), Finite strain estimation using mean radial length of elliptical objects with bootstrap confidence intervals, *J. Struct. Geol.*, *25*, 529–539.

Okudaira, T., T. Takeshita, and M. Toriumi (1998), Discussion: Prism- and basal-plane parallel subgrain boundaries in quartz: a microstructural geothermometer (paper by Kruhl, 1996), *J. Metamorph. Geol.*, *16*, 141–146.

Okudaira, T., T. Takeshita, I. Hara, and J.-I. Ando (1995), A new estimate of the conditions for transition from basal $a >$ to prism [c] slip in naturally deformed quartz, *Tectonophysics*, *250*, 31–46.

Ollier, C. D., and C. F. Pain (1980), Active rising surficial gneiss domes in Papua New Guinea, *J. Geol. Soc. Aust.*, *27*, 33–44.

Olsen, T. S., and D. L. Kohlstedt (1985), Natural deformation and recrystallization of some intermediate plagioclase feldspars, *Tectonophysics*, *111*, 107–131.

Ota, T., and Y. Koneko (2010), Blueschists, eclogites, and subduction zone tectonics: Insights from a review of Late Miocene blueschists and eclogites, and related young high-pressure metamorphic rocks, *Gondwana Res.*, *18*, 167–188.

Pennacchioni, G., L. Menegon, B. Leiss, F. Nestola, and G. Bromiley (2010), Development of crystallographic preferred orientation and microstructure during plastic deformation of

natural coarse-grained quartz veins, *J. Geophys. Res.*, *115*, B12405, 12423 pp.

Piazolo, S., M. Bestmann, D. J. Prior, and C. J. Spiers (2006), Temperature dependant grain boundary migration in deformed-then-annealed material: Observations from experimentally deformed synthetic rock salt, *Tectonophysics*, *427*, 55–71.

Platt, J. P., and W. M. Behr (2011), Grainsize evolution in ductile shear zones: Implications for strain localization and the strength of the lithosphere, *J. Struct. Geol.*, *33*(4), 537–550.

Pryer, L. L. (1993), Microstructures in feldspars from a major crustal shear zone: the Grenville Front, Ontario, Canada, *J. Struct. Geol.*, *15*, 21–36.

Robertson, A. H. F., S. A. M. Awadallah, S. Gerbaudo, K. S. Lackschewitz, B. Monteleone, T. R. Sharp, and O. L. S. S. Party (2001), Evolution of the Miocene-Recent Woodlark Rift Basin, SW Pacific, inferred from sediments drilled during Ocean Drilling Program Leg 180, in *Nonvolcanic Rifting of Continental Margins: A Comparison of Evidence from Land and Sea*, edited by R. C. L. Wilson, N. Frotzheim, B. Tatylor, and R. B. Whitmarsh, pp. 335–372, Geological Society of London Special Publication, London U.K.

Rogerson, R., D. Hilyard, E. J. Finalyson, D. S. Holland, S. T. S. Nion, R. S. Sumaiang, J. Duguman, and C. D. C. Loxton (1987), *The geology and mineral resources of the Sepik headwaters region*, Papua New Guinea, *Papua New Guinea Geological Surveys Memoir 12*.

Rosenberg, C. L., and H. Stunitz (2003), Deformation and recrystallization of plagioclase along a temperature gradient: and example from the Bergell tonalite, *J. Struct. Geol.*, *25*, 389–408.

Rosenberg, C. L., and M. R. Handy (2005), Experimental deformation of partially melted granite revisited: Implications for the continental crust, *J. Metamorph. Geol.*, *23*, 19–28.

Rybacki, E., and G. Dresen (2004), Deformation mechanism maps for feldspar rocks, *Tectonophysics*, *382*, 173–187.

Schmid, S. M., and M. Casey (1986), Complete fabric analysis of some commonly observed quartz c-axis patterns, in *Mineral and Rock Deformation: Laboratory Studies— The Paterson Volume*, edited by B. E. Hobbs and H. C. Heard, pp. 263–286 American Geophysical Union Geophysical Monograph Series vol 36, Washinton D.C. USA.

Skemer, P., I. Katayama, Z. Jiang, and S. Karato (2005), The misorientation index: Development of a new method for calculating the strength of lattice-preferred orientation, *Tectonophysics*, *411*, 157–167.

Smith, I. E., and H. L. Davies (1976), Geology of the southeast Papuan Mainland, *Aust. BMR Geol. Geophys. Bull.*, *165*, 32.

Stipp, M., H. Stunitz, R. Heilbronner, and S. M. Schmid (2002a), The eastern Tonale fault zone: a "natural laboratory" for crystal plastic deformation of quartz over a temperature range from 250 to 700°C, *J. Struct. Geol.*, *24*, 1861–1884.

Stipp, M., H. Stunitz, R. Heilbronner, and S. M. Schmid (2002b), Dynamic recrystallization of quartz: correlation between natural and experimental conditions, in *Deformation Mechanisms, Rheology, and Tectonics: Current Status and Future Perspectives*, edited by S. De Meer, M. R. Drury, J. H. P. De Bresser and G. M. Pennock, pp. 171–190, Geol. Soc. London Spec. Publication 200, London U.K..

Stipp, M., and J. Tullis (2003), The recrystallized grain size piezometer for quartz, *Geophys. Res. Lett.*, *30*, 2088, *Geol. Soc.* London Spec Publication 200, London, U.K., doi:10.1029/2003GL018444.

Stipp, M., J. Tullis, M. Scherwath, and J. H. Behrmann (2010), A new perspective on paleopiezometry: Dynamically recrystallized grain size distributions indicate mechanism changes, *Geology*, *38*, 759–762.

Stöckhert, B. (2002), Stress and deformation in subduction zones- insight from the record of exhumed high pressure metamorphic rocks, in *Deformation Mechanisms, Rheology and Tectonics: Current Status and Future Perspectives*, edited by S. De Meer, M. Drury, H. De Bresser, and G. Pennock, pp. 255–274, Geological Society of London Special Publication 200, London, U.K.

Takeshita, T. (1996), Estimate of physical conditions for deformation based on c-axis transitions in naturally deformed quartzite, *J. Geol. Soc. Japan*, *102*(3), 211–222.

Taylor, B., and P. Huchon (2002), Active continental extension in the western Woodlark basin: A synthesis of Leg 180 results, in *Proceedings of the Ocean Drilling Program, Scientific Results Volume 180*, edited by P. Huchon, B. Taylor and A. Klaus, pp. 1–36 (CD ROM), Ocean Drilling Program, Texas A & M University, College Station, TX.

Taylor, B., A. M. Goodliffe, and F. Martinez (1999), How Continents break-up: Insights from Papua New Guinea, *J. Geophys. Res.*, *104*, 7497–7512.

ten Grotenhuis, S. M., R. A. J. Trouw, and C. W. Passchier (2003), Evolution of mica fish in mylonitic rocks, *Tectonophysics*, *372*, 1–21.

Toy, V. G., D. J. Prior, and R. J. Norris (2008), Quartz fabrics in the Alpine Fault mylonites: Influence of pre-existing preferred orientations on fabric development during progressive uplift, *J. Struct. Geol.*, *30*(5), 602–621.

Tullis, J. (2002), Deformation of granitic rocks: Experimental studies and natural examples, in *Plastic Deformation of Minerals and Rocks*, edited by S. Karato and H.-R. Wenk, pp. 51–95, Mineralogical Society of America, Washington, D. C.

Tullis, J., J. M. Christie, and D. T. Griggs (1973), Microstructures and preferred orientations of experimentally deformed quartz-ites, *Geol. Soc. Am. Bull.*, *84*, 297–314.

Urai, J. L., W. D. Means, and G. S. Lister (1986), Dynamic recrystallization of minerals, in *Mineral and Rock Deformation: Laboratory Studies, the Paterson Volume*, edited by B. E. Hobbs and H. C. Heard, pp. 161–200, American Geophysical Union, Washington, D. C.

Van Ufford, Q. A., and M. Cloos (2005), Cenozoic tectonics of New Guinea, *Am. Assoc. Pet. Geol. Bull.*, *89*, 119–140.

Vidal, J. L., L. Kubin, P. Debat, and J. L. Soula (1980), Deformation and dynamic recrystallization of K-feldspar augen in orthogneiss from Montagne Noir, Occitania, *Lithos*, *13*, 247–257.

Waggoner, A., S. L. Baldwin, L. A. Webb, T. A. Little, and P. G. Fitzgerald (2008), Temporal constraints on continental rifting and the exhumation of the youngest known HP metamorphic rocks, SE Papua New Guinea, in *Annual Meeting of the American Geophysical Union*, edited, pp. T41B–1961, EOS Transactions, San Francisco, CA.

Wark, D. A., and E. B. Watson (2006), TitaniQ: a titanium-in-quartz geothermometer, Contributions to Mineralogy and Petrology, *152*, 743–754.

Wallace, L. M., C. Stevens, E. Silver, R. McCaffrey, W. Loratung, S. Hasiata, R. Stanaway, R. Curley, R. Rosa, and J. Taugaloidi (2004), GPS and seismological constraints on active tectonics and arc-continent collision in Papua New Guinea: Implications for mechanics of microplate rotations in a plate boundary zone, *J. Geophys. Res.*, *109*(B05404). doi:10.1029/2003JB002481.

Warren, C. J. (2012), Up the down escalator: the exhumation of (ultra)-high pressure terranes during ongoing subduction, *Solid Earth Discuss.*, *4*, 745–781.

Webb, L. E., S. L. Baldwin, T. A. Little, and P. G. Fitzgerald (2008), Can microplate rotation drive subduction inversion?, *Geology*, *36*, 823–826.

Westaway, R. (2005), Active low-angle normal faulting in the Woodlark extensional province, Papua New Guinea: A physical model, *Tectonics*, *24*, TC6003, doi:10.1029/2004TC001744.

Whitney, D. L., C. Teyssier, and O. Vanderhaeghe (2004), Gneiss domes and crustal flow, in *Gneiss Domes in Orogeny*, edited by D. L. Whitney, C. Teyssier, and C. S. Siddoway, pp. 15–33, Geological Society of America, Boulder, CO.

Wintsch, R. P., and K. Yi (2002), Disslution and replacement creep: a significant defeormation mechanism in mid0crustal rocks, *J. Struct. Geol.*, *24*, 1179–1193.

Worthing, M. A., and A. J. Crawford (1996), The igneous geochemistry and tectonic setting of metabasites from the Emo metamorphics, Papua New Guinea: the record of the evolution and destruction of a back-arc basin, *Mineral. Petrol.*, *58*, 79–100.

Yin, A. (2004), Gneiss domes and gneiss dome systems, in *Gneiss Domes in Orogeny*, edited by D. L. Whitney, C. Teyssier and C. S. Siddoway, pp. 1–14, Geological Soociety of America, Boulder, Colorado.

Zavada, P., K. Schulmann, J. Konopasek, S. Ulrich, and O. Lexa (2007), Extreme ductility of feldspar aggregates– melt enhanced grain boundary sliding and creep failure: Rheological implications for felsic lower crust>, *J. Geophys. Res.*, *112*, B10210.

Zibra, I., J. H. Kruhl, A. Montanini, and R. Tribuzio (2012), Shearing of magma along a high-grade shear zone: Evolution of microstructures during the transition from magmatic to solid-state flow, *J. Struct. Geol.*, *37*, 150–160.

Zirakparvar, N. A., et al. (2013), The origin and geochemical evolution of the Woodlark Rift of Papua New Guinea, *Gondwana Res.*, *23*, 931–943.